University of Nebraska - Lincoln
DigitalCommons@University of Nebraska - Lincoln

US Department of Energy Publications | U.S. Department of Energy

2003

Desorption kinetics of radiocesium from subsurface sediments at Hanford Site, USA

Chongxuan Liu
Pacific Northwest National Laboratory, chongxuan.liu@pnl.gov

John M. Zachara
Pacific Northwest National Laboratory, john.zachara@pnl.gov

Steven Smith
Pacific Northwest National Laboratory, steven.smith@pnl.gov

James Mckinley
Pacific Northwest National Laboratory, james.mckinley@pnl.gov

Calvin Ainsworth
Pacific Northwest National Laboratory

Follow this and additional works at: http://digitalcommons.unl.edu/usdoepub

 Part of the Bioresource and Agricultural Engineering Commons

Liu, Chongxuan; Zachara, John M.; Smith, Steven; Mckinley, James; and Ainsworth, Calvin, "Desorption kinetics of radiocesium from subsurface sediments at Hanford Site, USA" (2003). *US Department of Energy Publications*. 252.
http://digitalcommons.unl.edu/usdoepub/252

This Article is brought to you for free and open access by the U.S. Department of Energy at DigitalCommons@University of Nebraska - Lincoln. It has been accepted for inclusion in US Department of Energy Publications by an authorized administrator of DigitalCommons@University of Nebraska - Lincoln.

This article is a U.S. government work, and is not subject to copyright in the United States.

Pergamon

Geochimica et Cosmochimica Acta, Vol. 67, No. 16, pp. 2893–2912, 2003
Copyright © 2003 Elsevier Ltd
Printed in the USA. All rights reserved
0016-7037/03 $30.00 + .00

doi:10.1016/S0016-7037(00)00267-9

Desorption kinetics of radiocesium from subsurface sediments at Hanford Site, USA

CHONGXUAN LIU,* JOHN M. ZACHARA, STEVE C. SMITH, JAMES P. MCKINLEY, and CALVIN C. AINSWORTH
Pacific Northwest National Laboratory, P.O. Box 999, MSIN K8-96, Richland, WA 99352, USA

(*Received September* 25, 2002; *accepted in revised form April* 16, 2003)

Abstract—The desorption of $^{137}Cs^+$ was investigated on sediments from the United States Hanford site. Pristine sediments and ones that were contaminated by the accidental release of alkaline $^{137}Cs^+$-containing high level nuclear wastes (HLW, 2×10^6 to 6×10^7 pCi $^{137}Cs^+$/g) were studied. The desorption of $^{137}Cs^+$ was measured in Na^+, K^+, Rb^+, and NH_4^+ electrolytes of variable concentration and pH, and in presence of a strong Cs^+-specific sorbent (self-assembled monolayer on a mesoporous support, SAMMS). $^{137}Cs^+$ desorption from the HLW-contaminated Hanford sediments exhibited two distinct phases: an initial instantaneous release followed by a slow kinetic process. The extent of $^{137}Cs^+$ desorption increased with increasing electrolyte concentration and followed a trend of $Rb^+ \geq K^+ > Na^+$ at circumneutral pH. This trend followed the respective selectivities of these cations for the sediment. The extent and rate of $^{137}Cs^+$ desorption was influenced by surface armoring, intraparticle diffusion, and the collapse of edge-interlayer sites in solutions containing K^+, Rb^+, or NH_4^+. Scanning electron microscopic analysis revealed HLW-induced precipitation of secondary aluminosilicates on the edges and basal planes of micaceous minerals that were primary Cs^+ sorbents. The removal of these precipitates by acidified ammonium oxalate extraction significantly increased the long-term desorption rate and extent. X-ray microprobe analyses of Cs^+-sorbed micas showed that the $^{137}Cs^+$ distributed not only on mica edges, but also within internal channels parallel to the basal plane, implying intraparticle diffusive migration of $^{137}Cs^+$. Controlled desorption experiments using Cs^+-spiked pristine sediment indicated that the $^{137}Cs^+$ diffusion rate was fast in Na^+-electrolyte, but much slower in the presence of K^+ or Rb^+, suggesting an effect of edge-interlayer collapse. An intraparticle diffusion model coupled with a two-site cation exchange model was used to interpret the experimental results. Model simulations suggested that about 40% of total sorbed $^{137}Cs^+$ was exchangeable, including equilibrium and kinetic desorbable pools. At pH 3, this ratio increased to 60–80%. The remainder of the sorbed $^{137}Cs^+$ was fixed or desorbed at much slower rate than our experiments could detect. *Copyright © 2003 Elsevier Ltd*

1. INTRODUCTION

Cesium-137 is produced in high yield by fission of ^{238}U, and is a common contaminant resulting from nuclear weapons testing and nuclear fuels reprocessing. The aqueous concentration and subsurface migration of $^{137}Cs^+$ is controlled by its strong sorption to and desorption from soils and sediments. Cesium sorption and desorption is influenced by sorbent properties, such as mineralogy and cation exchange capacity (CEC), competing cations, such as Na^+ and K^+, and age of the sorption complex. An understanding of the Cs^+ sorption/desorption process is important for evaluating the environmental risks associated with the radiocesium migration and the feasibility of remediation strategies.

Cs^+ sorption occurs primarily by ion exchange to the phyllosilicate fraction of soil or sediment. Experimentally measured Cs^+-exchange isotherms often imply the presence of two or more sites with distinctive exchange energies (Sawhney, 1972; Brouwer et al., 1983; Cornell, 1993; Zachara et al., 2002). The high-energy site is believed to be associated with frayed-edge regions of weathered 1.0 nm micaceous minerals, and the low energy sites with the basal planes of expansible phyllosilicates including smectite and vermiculite. The presence of multiple sorption sites has been generally confirmed by NMR studies of Cs^+-exchanged clay minerals (Weiss et al., 1990a,b; Kim et al., 1996). The short-term sorption/exchange of Cs^+ often exhibits reversible behavior (Brouwer et al., 1983; Zachara et al., 2002), and has been described by multi-site, equilibrium exchange models (Brouwer et al., 1983; Cremers et al., 1988; Poinssot et al., 1999; Steefel et al., 2002; Zachara et al., 2002).

The sorption and desorption of Cs^+ can exhibit kinetic behavior over longer contact periods (Evans et al., 1983; Di Toro et al., 1986; De Preter, 1990; Comans et al., 1991). Slow diffusion of Cs^+ within edge-interlayer regions of micaceous minerals, accentuated by layer collapse around the poorly hydrated Cs^+ ion, is believed to cause this kinetic phenomenon (Sawhney, 1967, 1969, 1972; Eberl, 1980). Such diffusion may take days, months, years, or even decades for sorption/desorption to reach the equilibrium state depending on the structure of the mineral sorbents and the aqueous composition (Evans et al., 1983; Di Toro et al., 1986; De Preter, 1990; Comans et al., 1991).

Edge and/or interlayer collapse on phyllosilicate sorbents slows Cs^+ desorption leading to exchange irreversibility or fixation (e.g., Sawhney, 1972; Evans et al., 1983; De Preter, 1990; Comans et al., 1991). Debate exists whether "fixed" Cs^+ is, or is not, exchangeable at slow rate (Comans et al., 1991; Cornell, 1993). The sorption of other exchangeable cations with low hydration energy, such as K^+, Rb^+, and NH_4^+, may also collapse the edge-interlayer region, decreasing Cs^+ adsorption and desorption rate (Sawhney, 1967, 1972; Le Roux et al., 1970). In contrast, strongly hydrated cations (e.g., Na^+ and Ca^{2+}) may expand the edge-interlayer region—inducing an opposite effect.

* Author to whom correspondence should be addressed (chongxuan.liu@pnl.gov).

The phenomenological aspects of Cs^+ desorption are understood primarily from investigations of single-phase 2:1 layer silicates. Comparable studies of Cs^+-contaminated soil and sediment are relatively rare. Long-term exposure allows Cs^+ diffusion into edge-interlayer regions of micaceous sorbents. Limited study suggests that desorption rate and extent decreases with contact time (Evans et al., 1983; Smith and Comans, 1996), but controlling features and parameters are not understood. Understanding Cs^+ desorption from natural sediments subjected to long-term contamination is key to predicting future Cs^+ migration.

In this communication, we investigate factors controlling Cs^+ desorption from micaceous sediments that were contaminated with a $^{137}Cs^+$-enriched high-level nuclear waste (HLW) stream over 30 yr ago. The HLW was geochemically reactive (high $[Na^+]$ and $[OH^-]$, temperature $>70°C$), inducing both dissolution and precipitation reactions upon sediment contact that moderated with distance from the waste source. A series of sediment samples collected with increasing distance from the waste source and varying in sorbed $^{137}Cs^+$ concentration were contacted with different electrolytes (Na^+, K^+, NH_4^+, and Rb^+) and a Cs^+-specific sorbent to quantify desorption rate and extent. Scanning electron and X-ray microscopy was applied to identify the degree of mineral alteration and Cs^+-sorption location. Equilibrium and kinetic modeling was used to quantify ion exchange mass action effects, and to derive mass transfer parameters consistent with data trends. Secondary mineral precipitation, intraparticle diffusion, and edge collapse all appear to influence the release of $^{137}Cs^+$ from the contaminated sediments and insights are provided on their relative importance.

2. EXPERIMENTAL PROCEDURES

2.1. Sediment Collection and Analysis

$^{137}Cs^+$-contaminated sediments were obtained from two boreholes (SX-108, 41-09-39) in the Hanford S-SX tank farm and included SX-108 samples 3A (20.6 m below ground surface [bgs]) and 7A (25.8 m bgs), and 41-09-39 samples 7ABC (25.3 m bgs) and 9ABC (22.8 m bgs). The collection and analyses of the sediments was described elsewhere (Serne et al., 2001a,b). Subsamples of the field moist materials were air-dried to a constant weight and sieved to pass a 2 mm mesh. Gravels >2 mm were removed from the air-dried materials during the sieving process. The sieved materials were mixed as well as possible given their high radioactivity to obtain a homogenized sample.

Pristine sediments from comparable depth intervals were obtained from four RCRA monitoring wells surrounding the S-SX tank farm (Zachara et al., 2002) for use in controlled experiments of Cs^+ ion exchange and desorption. The pristine materials were treated in the same manner as the contaminated materials described above. The homogenized pristine sediments were termed the "Above B" composite. Both the pristine and contaminated sediments were obtained from the upper Hanford formation, which is a Pleistocene-age, catastrophic flood deposit. The mineralogical compositions of the pristine and contaminated sediments were the same except that the contaminated sediments were altered by HLW-sediment reaction.

The contaminated sediment contained a high level of residual salt ($NaNO_3$) from the HLW. Before drying, the moisture content of the sediment ranged between 2.8–6.2%, and the pore-water concentration of $NaNO_3$ associated with this moisture context ranged between 5 and 15 mol/L (Liu et al., 2003). These pore-water concentrations were estimated by 1:1 deionized water extraction of the sediment (Serne et al., 2001a,b).

2.2. Mass Action Effects on $^{137}Cs^+$ Desorption

Air-dried, sieved contaminated sediment (2 g) was weighed into a 30 mL Oakridge polycarbonate centrifuge tube containing 4 mL of either 0.05, 0.5 or 5 mol/L $NaNO_3$, or 0.05, 0.5 or 3.4 mol/L KNO_3 or $RbNO_3$. After equilibration for 6 d at 25°C under continuous mixing, the suspensions were centrifuged at 5000 rcf (relative centrifugal force) for 30 min and supernatant (0.5 mL) was transferred to a preweighed gamma count vial and reweighed. The $^{137}Cs^+$ activity of the sample was counted for 30 min using a Wallac gamma counter, model 1480 with an 76 mm NaI crystal detector. The count window was set at 560 to 710 keV yielding a count efficiency of 0.207.

2.3. Cation Exchange Capacity (CEC)

Following the measurement of $^{137}Cs^+_{(aq)}$ in the 6 d equilibration with 0.05, 0.5, or 5 mol/L $NaNO_3$, the supernate was removed and replaced with 12 mL of 5 mol/L $NaNO_3$. The sediment was washed four times with 5 mol/L Na^+. The Na^+-treated sediments were then washed with 12 mL of deionized water for 2 d, and with 12 mL of 0.05 mol/L Na^+ for 2 d. After the last wash, 4 mL of sediment suspension in 0.05 mol/L Na^+ was mixed with 16 mL of $^{22}Na^+$ in water (approximately 20,000 dpm/mL). After 16 h of equilibration, the suspensions were centrifuged (5000 rcf for 30 min) and the ^{22}Na activity was determined in the supernatants. The Na^+-cation exchange capacity was calculated from the initial and final $^{22}Na^+$counts in solution, and the aqueous Na^+ concentration. Aqueous Na^+ in 0.2 μm filtrate was determined by inductively coupled plasma-optical emission spectroscopy (ICP-OES).

The Cs^+-cation exchange capacity was similarly determined. The sediments in the suspensions with 0.05, 0.5, or 5 mol/L $NaNO_3$ were repeatedly washed with 1 mol/L $CsNO_3$, followed by two washes with deionized water, and two washes with 0.05 mol/L $CsNO_3$. The 4 mL of sediment suspension at 0.05 mol/L $CsNO_3$ was mixed with 16 mL of $^{134}Cs^+$. After equilibration and centrifugation, the supernatants of the suspensions were filtered (0.2 μm) for ICP-OES measurement of aqueous Cs^+ and measurement of $^{134}Cs^+$ activity.

2.4. $^{137}Cs^+$ Desorption Kinetics

Two replicates of air-dried contaminated sediment (0.5 g) were weighed into 30 mL Oakridge polycarbonate centrifuge tubes and mixed with 5 mL of 0.5 mol/L KNO_3, $RbNO_3$, or NH_4NO_3. The suspensions were equilibrated with continual gentle mixing. At selected times, the suspensions were centrifuged (5000 rcf for 10 min) and 0.5 mL of supernatant was transferred to a preweighed gamma count vial and reweighed.

The aqueous $^{137}Cs^+$ activity was measured as previously described. Following the determination of $^{137}Cs^+$ activity, the subsample was returned to the suspension to maintain a constant solid to solution ratio. The final sampling time at 0.5 mol/L electrolyte was 47 d in KNO_3 and $RbNO_3$, and 56 d in NH_4NO_3.

Following the 47 d of equilibration with 0.5 mol/L of K^+ or Rb^+ electrolyte, the electrolyte concentration was increased to 2 mol/L to evaluate the mass action effect on desorption kinetics. This was accomplished by transferring approximately 4 mL of each supernatant to a plastic tube containing a preweighed mass of dry KNO_3 or $RbNO_3$ necessary to raise the electrolyte concentration to the desired level without changing the solid to solution ratio. The added salt was dissolved within 2 h and the solutions were transferred back to their original containers for equilibration. At selected times, the suspension solution was sampled for aqueous $^{137}Cs^+$ as previously described and returned to the suspension. Following the 65 d of equilibration the supernatants were filtered (0.2 μm) for ICP-OES analysis of K^+ or Rb^+ concentrations.

2.5. $^{137}Cs^+$ Desorption Kinetics in Acidified Ammonium Oxalate (pH 3)

The contaminated sediments were contacted with ammonium oxalate at pH 3 to determine if poorly crystalline precipitates of Fe(III) and Al(III) resulting from waste-sediment reaction affected $^{137}Cs^+$ desorption rate and extent. Replicate suspensions of each contaminated sediment (0.5 g) were prepared in 0.25 mol/L $(NH_4)_2$-oxalate at pH 3 (5 mL) and sampled at select time points up to 134 d. Phase separation was performed by centrifugation (5000 rcf for 30 min) and filtration (0.2 μm). The first 1 mL of filtrate was discarded and the remaining collected in a plastic tube. Aqueous $^{137}Cs^+$ was determined as previously described. Other elements in the filtrate (Fe, Al, Ba, Ca, Cr, K, Mg, Na, and Si) were analyzed using ICP-OES. Suspension pH was measured using a Microelectrodes combination pH electrode.

2.6. $^{137}Cs^+$ Desorption Induced by a Competitive Sorbent

A Cs-specific sorbent, self-assembled monolayer on mesoporous support (SAMMS) (Lin et al., 2001), was used to expedite $^{137}Cs^+$ desorption. The SAMMS contains an immobilized ferrocyanide complexant group for Cs^+ on a mesoporous, high surface area silica support. It has a property of high sorption capacity (1.35 mmol/g) and fast sorption kinetics (Lin et al., 2001). Approximately one gram of SX-108 7A sediment was transferred to cellulose dialysis membrane tubing (SpectraPor 7, 1000 MWCO) containing 5 mL of either 1 or 0.01 mol/L $NaNO_3$. The membrane tubing was tightly sealed and placed in 95 mL of the same electrolyte in a 250 mL polycarbonate bottle. The bottle was placed on an end-over-end mixer (18 cm radius, 3 rpm). The lysate solution was periodically sampled, counted for ^{137}Cs-activity, and returned to the reaction vessel. After steady state conditions were achieved (approximately 4 d), SAMMS in deionized water were added to the solution outside the dialysis tubing to yield 0.05 g/L. At selected time intervals, 0.5 mL of the electrolyte with SAMMS was removed and counted for total ^{137}Cs-activity, then returned to the reaction vessel. Additionally, at selected time points, 1.0 mL of the electrolyte with SAMMS was filtered (0.2 μm). The first 8 drops of the filtrate were discarded and 0.5 mL of the filtrate was collected and counted for aqueous $^{137}Cs^+$-activity. After approximately 9 d, additional SAMMS was added to the suspension to yield 0.25 g/L. The suspension was sampled as described above.

2.7. Ion exchange of Cs^+-Rb^+, Cs^+-NH_4^+, and Rb^+-Na^+ on Pristine Sediment

The ion exchange behavior of Cs^+ relative to the displacing cations was determined to parameterize the mass action process for development of a kinetic desorption model. The uncontaminated "Above B" sediment was used as an analog to the contaminated one to avoid the interference of other processes in the interpretation of experimental results. Some of the necessary ion exchange data had already been measured [e.g., Cs^+-Na^+, Cs^+-K^+; (Zachara et al., 2002)] and was not repeated here. The "Above B" sediment was treated with 1 mol/L sodium acetate (NaOAc) at pH 5.0 (with acetic acid) to remove carbonates and soluble salts (Zachara et al., 2002). The ion exchange behavior of Cs^+-Rb^+ and Cs^+-NH_4^+ was measured in 0.05 mol/L $RbNO_3$ and 0.5 mol/L NH_4NO_3. The sediments were washed three times in the appropriate electrolyte (Rb^+ or NH_4^+) and resuspended before addition of $CsNO_3$. The $CsNO_3$ concentrations ranged from 10^{-9} to 10^{-1} mol/L, and were labeled with 7.0×10^3 to 2.0×10^4 dpm/mL $^{137}Cs^+$. The ion exchange behavior of Rb^+-Na^+ was measured in 0.01, 0.1, and 1 mol/L $NaNO_3$ electrolytes with Na^+-saturated sediment and a Rb^+ concentration range of 10^{-9} to 10^{-2} mol/L. An $^{86}Rb^+$ label was used to trace the partitioning of Rb^+ between the aqueous and solid phases. The suspensions were shaken in 30 mL Oakridge polycarbonate tubes at 40 rpm and 25°C for 16 h. After equilibration, the suspensions were centrifuged and the supernatants were measured for $^{137}Cs^+$ and $^{86}Rb^+$ activities.

2.8. Kinetic Studies of Adsorption/Desorption of Cs^+ on Pristine Sediments

The NaOAc-treated "Above B" sediment was used to study the kinetics of the short-term Cs^+ adsorption/desorption process in the absence of secondary mineral products of HLW-sediment reaction. The sorption experiments were performed in 0.1 mol/L $NaNO_3$ electrolyte spiked with 3.2×10^{-7} mol/L $CsNO_3$. The solution was labeled with $^{137}Cs^+$ and mixed with 10 g/L sediment in a 30 mL Oakridge polycarbonate tube. The suspensions were equilibrated at room temperature on a bench top shaker at 100 rpm. At selected time points, the suspensions were centrifuged and $^{137}Cs^+$ was measured as previously described to quantify the time-dependent sorption process.

The Cs^+-loaded "Above B" sediments were used for desorption experiments and were mixed with 5 mol/L $NaNO_3$, 2.9 mol/L $RbNO_3$, and 2.9 mol/L KNO_3 electrolytes at 50 g/L solid concentration. Two sets of desorption experiments were performed. One used the sediments after 1 d of Cs^+ adsorption and followed Cs^+ desorption with time. The other used the sediments after variable days of Cs^+ adsorption and measured Cs^+ desorption after 1 d equilibration. The equilibration, phase separation, and γ-counting were performed as described above.

Table 1. Cs^+ concentration and cation exchange capacity (CEC) on the contaminated S-SX sediments.

	SX-108-3A	SX-108-7A	41-09-39-7ABC	41-09-39-9ABC
$^{137}Cs^+$ (pCi/g)[a]	3.420×10^7	5.937×10^7	4.009×10^7	2.195×10^6
Total Cs^+ (μmol/g)[b]	1.366×10^{-2}	2.372×10^{-2}	1.601×10^{-2}	8.768×10^{-4}
CEC (μEq/g of dry sediment) determined using $^{134}Cs^+$	49.8 ± 0.5	74.9 ± 5.7	61.2 ± 3.3	46.1 ± 2.8
CEC (μEq/g of dry sediment) determined using $^{22}Na^+$	44.4 ± 0.7	63.2 ± 2.7	51.0 ± 1.7	38.8 ± 2.6
Fractional occupation of high-affinity site[c]	0.61	0.70	0.58	0.42

[a] Determined by gamma count, including those in solid and pore-water phases.
[b] Total Cs^+ calculated based on $^{137}Cs^+$ concentrations using Eqns. 1 and 2.
[c] Calculated based on Cs-CEC and a fraction of high affinity sites to CEC (4.5×10^{-4}) (Zachara et al., 2002; Liu et al., 2003).

2.9. Spatial Distribution of Sorbed Cs^+in Micas from Pristine Sediment

Most of the radiocesium in the contaminated sediments (41-09-39) has been previously shown to associate with mica grains (biotite, partially vermiculitized biotite, muscovite) and smectite-cemented clasts (McKinley et al., 2001). Attempts to define a conceptual model for intragrain $^{137}Cs^+$ transport by spatially resolved X-ray microprobe measurements of micas separated from the contaminated sediment were unsuccessful because of the low molar adsorbed Cs^+ concentration (e.g., $< 10^{-7}$ mol/g) of the radioactively contaminated micas. As a surrogate, we hand picked mica grains from the "Above B" composite, contacted these with 10^{-3} mol/L $CsNO_3$ solutions, washed them with deionized H_2O, mounted the grains in Buehler petrographic epoxy, and made thin sections (ca. 60 μm) parallel to the C-axis. The thin sections were analyzed by X-ray microprobe (XRM) on the GSE-CARS beamline at the Advanced Photon Source (APS), Argonne National Laboratory (details given by McKinley et al., 2001). The observed spatial distribution of Cs^+ was considered qualitatively representative of the radiocesium distribution in contaminated micas.

2.10. Data Analysis

The speciation, activity coefficients, and water activity in the aqueous phase were assumed to be in equilibrium and were calculated for each sample using measured aqueous concentrations and a computerized chemical equilibrium program, GMIN (Felmy, 1995), which incorporated the Pitzer ion-ion interaction model (Pitzer, 1994) and Cs^+-electrolyte interaction constants summarized in Liu et al. (2003).

3. RESULTS

3.1. $^{137}Cs^+$ Concentration and CEC

The total $^{137}Cs^+$ activities in the HLW-contaminated sediments ranged from 2×10^6 to 6×10^7 pCi/g of dry sediment depending on the sample locations (Table 1). The total Cs^+ inventory of the sediments includes the Cs^+ isotopes 133 and 135 that were also part of HLW. The concentrations of different Cs isotopes were quantified by mass spectroscopy (Evans et al., 2001). The relationship between $^{137}Cs^+$ and total Cs^+ concentration in the sediments was:

$$Cs^+_{total}(\text{mol/g}) = 4.75(\pm 0.18)\, ^{137}Cs^+(\text{mol/g}) \quad (1)$$

The molar concentration is related to the activity of $^{137}Cs^+$ by:

$$^{137}Cs^+(\text{mol/g}) = {}^{137}Cs^+(\text{pCi/g}) * 2.22 * 365.25 * 24 * 60 * t_{1/2}/(\ln 2 * N_A) \quad (2)$$

where $t_{1/2}$ (year) is the half-life of $^{137}Cs^+$ decay (30.07 yr), and N_A is the Avogadro constant. The total Cs^+ concentrations in the sediment samples were calculated by Eqns. 1 and 2 using the measured $^{137}Cs^+$ activities (Table 1). Cs^+ isotopic compositions were also measured in selected supernates from the mass-action desorption experiments, and the desorbed Cs^+ pool exhibited the same isotopic ratios as the contaminated sediments (Evans et al., 2001). The concentration of $^{137}Cs^+$ was, therefore, used to trace the behavior of the total Cs^+ pool. All our reported analyses for $^{137}Cs^+$, therefore, represent 21.05% of the total Cs^+.

The CEC determined using both $^{134}Cs^+$ and $^{22}Na^+$ on the $^{137}Cs^+$-contaminated sediments ranged from 38.8 to 74.9 μEq/g of dry sediment (Table 1) and was comparable to that measured on the pristine "Above B" sediments (42.6 to 82.5 μEq/g of dry sediment) (Zachara et al., 2002). The CECs (Table 1) determined using $^{134}Cs^+$ were consistently higher than using $^{22}Na^+$, possibly due to the incomplete replacement of Cs^+ and K^+ in the sediment by Na^+ in spite of the aggressive washes of the sediments with Na^+-electrolyte. A similar problem was noted previously with K^+ (Zachara et al., 2002).

The sediment $^{137}Cs^+$ activity increased with CEC (Table 1). The ratio of the total Cs^+ concentration ($^{133}Cs^+ + {}^{135}Cs^+ + {}^{137}Cs^+$) to the CEC (either $^{22}Na^+$ or $^{134}Cs^+$) for all samples was less than 3.8×10^{-4}. This value was less than the fraction of high affinity sites calculated for the "Above B" sediment (4.5×10^{-4}) (Zachara et al., 2002; Liu et al., 2003). Apparently, adsorbed Cs^+ was associated primarily with high affinity ion exchange sites in the contaminated sediment. The total sediment Cs^+ concentrations were ~42 to 70% of the high affinity site capacity (Table 1).

3.2. Cation Selectivity Coefficients

The cation selectivity coefficients (K_v) for the binary exchange of Rb^+-Na^+, Cs^+-Rb^+, and Cs^+-NH_4^+ on the "Above B" sediments showed two-site exchange behavior (Fig. 1), as was observed previously (Zachara et al., 2002; Liu et al., 2003). The two-site exchange behavior was consistent with specific Cs^+ association to edge-interlayer regions of muscovite and biotite, and electrostatic association with vermiculite and smectite (McKinley et al., 2001; Zachara et al., 2002). Ion exchange studies on pure illite also show comparable compositional

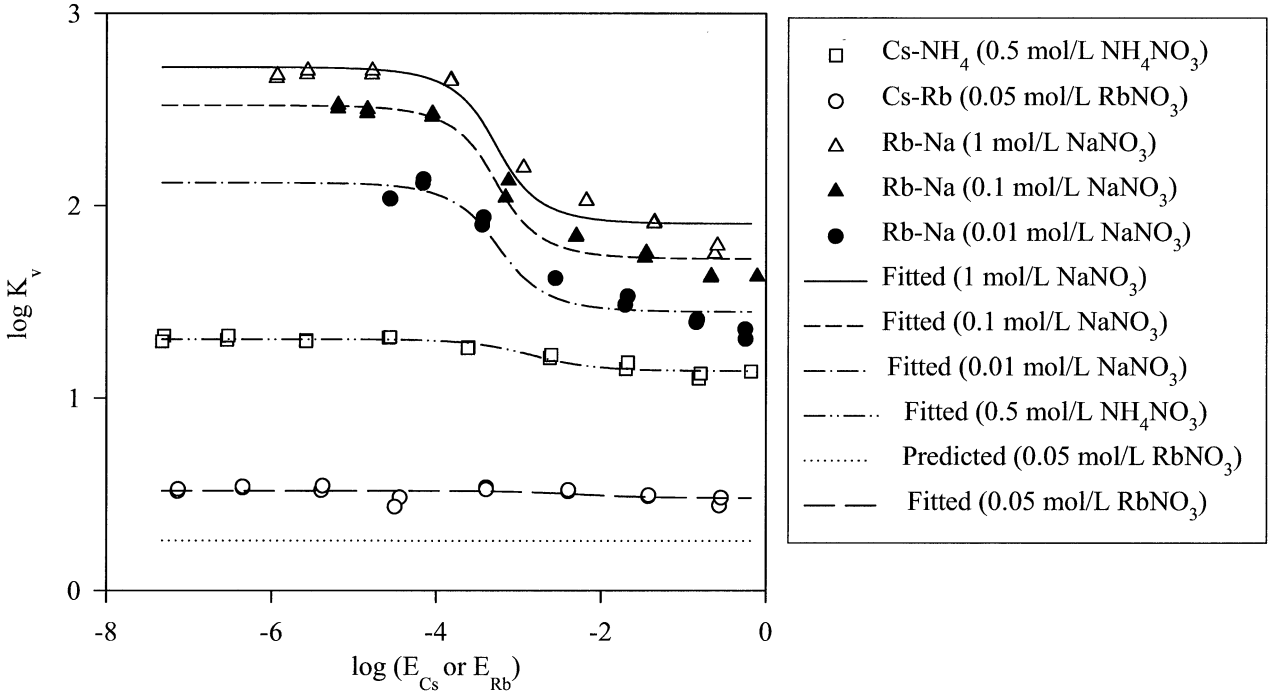

Fig. 1. Experimental and modeling results of cation exchange isotherms for different binary exchange systems. Each isotherm with the same ionic strength was fitted by a two-site model (text) with the fitted selectivity coefficients provided in Table 2. E_{Cs} and E_{Rb} are the equivalent fraction of Cs^+ and Rb^+, respectively. E_{Cs} used for Cs-NH_4 and Cs-Rb exchange, and E_{Rb} were used for Rb-Na exchange. The selectivity coefficient, K_v, was defined by Eqn. 3.

dependence and multi-site exchange behavior (Brouwer et al., 1983).

The mass action expression for ion exchange is commonly defined as

$$uB^{v+}_{(aq)} + vAX_u = uBX_v + vA^{u+}_{(aq)} \quad (3)$$

where u and v are the valences of ionic species A and B; AX_u and BX_v are the exchanger phase species A^{u+} and B^{v+}; and A^{u+} and B^{v+} are the aqueous species. The Vanselow selectivity coefficient (K_v) for the above ion exchange reaction may be defined as:

$$K_v = (N_B^u/N_A^v)(\{A^{u+}\}^v/\{B^{v+}\}^u) \quad (4)$$

where N_B and N_A are the mole fractions of exchanger phase species B^{v+} and A^{u+}; and {} denotes activity. The K_v is computed from the experimentally measurable conditional constant (K_c) corrected by aqueous speciation calculation. The conditional constant (for Cs^+ exchange) is defined as,

$$K_c = (N_{Cs}^u/N_A)([A^{u+}]/[Cs^+]^u) \quad (5)$$

where represents the concentration.

The selectivity coefficients (K_v, Fig. 1) were well described by a two-site exchange model (Table 2). The numerical procedures for the model were detailed elsewhere (Zachara et al., 2002). A CEC value of 82.5 μEq/g and a high affinity site fraction of 4.5×10^{-4} were assigned that were consistent with previous studies with this sediment (Zachara et al., 2002; Liu et al., 2003).

The selectivity coefficients for the ion exchange of Rb^+ for Na^+ increased with ionic strength (Fig. 1 and Table 2), as noted for Cs^+-Na^+ exchange on this same sediment (Liu et al., 2003). The ionic strength dependence is attributed to a water activity effect, and the large difference in ionic hydration energy between exchanging species (Barrer and Klinowski, 1974; Brouwer et al., 1983; Liu et al., 2003). A decrease in water activity at high ionic strength increases the binding energies of cations with low hydration energy, such as Rb^+ and Cs^+, to a greater extent than those with high hydration energy, such as Na^+ (Eberl, 1980). A thermodynamic model that included such binding energy changes with water activity was developed and applied to laboratory and field data for Cs^+-Na^+ exchange in these same S-SX sediments (Liu et al., 2003).

Because of the effects of ionic strength on the Rb^+-Na^+ exchange, the experimental results were simulated with a two-site exchange model corrected for the effects of water activity (Liu et al., 2003):

$$\log K_v^i(\ln a_w) = \log K_{ex}^i + k\sqrt{-\ln a_w}/(1+\sqrt{-\ln a_w}) \quad (6)$$

where a_w is the water activity; k is a fitting parameter to account for the magnitude of the effects of water activity on exchange selectivity, and K_v^i and K_{ex}^i are the selectivity and exchange constants at site i, respectively. Unlike K_v^i, $K_{ex}^i$is not a function of composition and electrolyte concentration, and is defined as,

$$K_{ex} = (\{BX_v\}^u/\{AX_u\}^v)/(\{A^{u+}\}^v/\{B^{v+}\}^u) \quad (7)$$

where all species are in activity. Eqn. 6 well described the

Table 2. Selectivity coefficients and exchange constants on Hanford "Above B" sediments.

Exchange reaction	Ionic strength (mol/L)	log $K_v^{I\,a}$	log $K_v^{II\,b}$
$Rb^+ + NaX = RbX + Na^+$	0.01	5.362 (0.050)	1.448 (0.028)
$Rb^+ + NaX = RbX + Na^+$	0.10	5.793 (0.032)	1.723 (0.022)
$Rb^+ + NaX = RbX + Na^+$	1.00	5.994 (0.043)	1.906 (0.035)
$Cs^+ + NaX = CsX + Na^+$	0.01	6.429 (0.064)	1.749 (0.043)
$Cs^+ + NaX = CsX + Na^+$	0.10	6.820 (0.052)	1.979 (0.039)
$Cs^+ + NaX = CsX + Na^+$	1.00	7.033 (0.047)	2.121 (0.041)
$Cs^+ + NaX = CsX + Na^+$	5.00	7.239 (0.029)	2.302 (0.028)
$Cs^+ + KX = CsX + K^+$	0.01	4.503 (0.024)	0.891 (0.012)
$Cs^+ + KX = CsX + K^+$	0.10	4.592 (0.024)	0.956 (0.008)
$Cs^+ + KX = CsX + K^+$	1.00	4.629 (0.024)	1.064 (0.009)
$Cs^+ + NH_4X = CsX + NH_4^+$	0.5	4.152 (0.028)	1.140 (0.008)
$Cs^+ + RbX = CsX + Rb^+$	0.05	2.780 (0.201)	0.480 (0.014)

Exchange reaction	k	log K_{ex}^{I}	log K_{ex}^{II}
$Cs^+ + NaX = CsX + Na^+$	2.26	6.637	1.761
$Cs^+ + KX = CsX + K^+$	1.14	4.502	0.889
$Cs^+ + RbX = CsX + Rb^+$	2.38	5.562	1.516

[a] High-affinity exchange sites.
[b] Low-affinity exchange sites.

experimental results of Rb^+-Na^+ exchange (results not shown, but they were close to the individual fittings in Fig. 1). The best-fit parameters are reported in Table 2. These parameters were determined by simultaneously fitting Eqn. 6 to the three isotherms of Rb^+ in Na^+ electrolyte (Fig. 1).

The selectivity coefficients for Rb^+-Na^+ exchange, together with the previously determined coefficients for Cs^+-Na^+ exchange (Table 2), allowed us to calculate the coefficients for Cs^+-Rb^+ exchange, log K_v^{I} (Cs-Rb) = log K_v^{I} (Cs-Na)log K_v^{I} (Rb-Na) = 1.039, 1027, and 1.067 and log K_v^{II} (Cs-Rb) = 0.215, 0.256, and 0.301, at 1, 0.1 0.01 mol/L electrolyte concentrations, respectively. Superscripts I and II represent the high and low affinity exchange sites, respectively. These values demonstrated that the ionic strength effect on Cs^+-Rb^+ exchange was negligible because of the similarity in ionic hydration energies of Cs^+ and Rb^+. These selectivity coefficients were comparable to those estimated on the high and low affinity sites on illite (Brouwer et al., 1983).

We used the calculated selectivity coefficients for Cs^+-Rb^+ exchange to predict the Cs^+ exchange isotherm in Rb^+ electrolyte (Fig. 1). The prediction consistently underestimated the experimental results in 0.05 mol/L $RbNO_3$ electrolyte by up to 0.25 log unit (Fig. 1). The reason for this underprediction was unclear. The best-fit selectivity coefficients for the Cs^+-Rb^+ exchange isotherm are summarized in Table 2.

3.3. Mass Action Effects on $^{137}Cs^+$ Desorption

The amount of $^{137}Cs^+$ desorbed after 6 d of equilibration increased with increasing concentrations of exchanging cations: Na^+, K^+, and Rb^+. The total desorption extent followed the trend: $Rb^+ > K^+ > Na^+$ (Fig. 2), as expected from the magnitude of the selectivity coefficients (Table 2). The amount of the Cs^+ desorbed in all samples and electrolytes, however, was less than 30% of the total Cs^+ on the sediments (Table 3).

A desorption ratio (D_r) was calculated from the measured 6-d aqueous $^{137}Cs^+$ concentration ($[^{137}Cs^+_{(aq)}]_{meas}$) and a model-predicted equilibrium aqueous $^{137}Cs^+$ concentration ($[^{137}Cs^+_{(aq)}]_{equil}$) based on the total Cs^+ content of each sample (Table 1): $D_r = [^{137}Cs^+_{(aq)}]_{meas}/[^{137}Cs^+_{(aq)}]_{equil}$. The model calculation used the Cs^+-CEC, the site fractions and selectivity coefficients for the "Above B" sediment (Table 2), and exchangeable concentrations of Na^+ and K^+ (Table 4, determined from the ammonium oxalate desorption experiments to be discussed subsequently). Ionic strength effects on the selectivity coefficients were corrected using Eqn. 6, and the Pitzer ion-ion interaction model (Pitzer, 1994) was used to calculate the activity of aqueous species. The D_r value was less than 0.3 in K^+ and Rb^+ electrolyte, but was 0.56 in 5 mol/L $NaNO_3$ (Table 3). The calculated ratios indicated that while K^+ and Rb^+ desorbed more $^{137}Cs^+$ from the sediment, their end states were further from equilibrium than was the Na^+ electrolyte system. None of the electrolyte systems achieved equilibrium in 6 d indicating that Cs^+ desorption was mass transfer limited.

3.4. $^{137}Cs^+$ Desorption Kinetics from the Contaminated Sediments

$^{137}Cs^+$ desorption showed a rapid initial release followed by a slow kinetic process (Fig. 3) in all sediment samples. Replicate solid samples showed excellent reproducibility for samples from borehole SX-108 (e.g., Figs. 3a,b), but less so for samples from borehole 41-09-39 (Figs. 3c,d). The greatest difference between replicates was for the 9ABC samples in Rb^+ electrolyte (Fig. 3d). The disparity between the K^+ and Rb^+ replicates in sample 7ABC and 9ABC was attributed to subsample inhomogeneity (e.g., the replicates varied in their total content of $^{137}Cs^+$ by as much as 50%). The coarse texture and aggregation status of the 41-09-39 samples, and the very high radioactivity of all the samples, complicated homogenization and subsampling activities. An increase in the displacing cation concentrations from 0.5 to 2 mol/L at 47 d induced another immediate increase of $^{137}Cs^+$ desorption (Fig. 3), followed

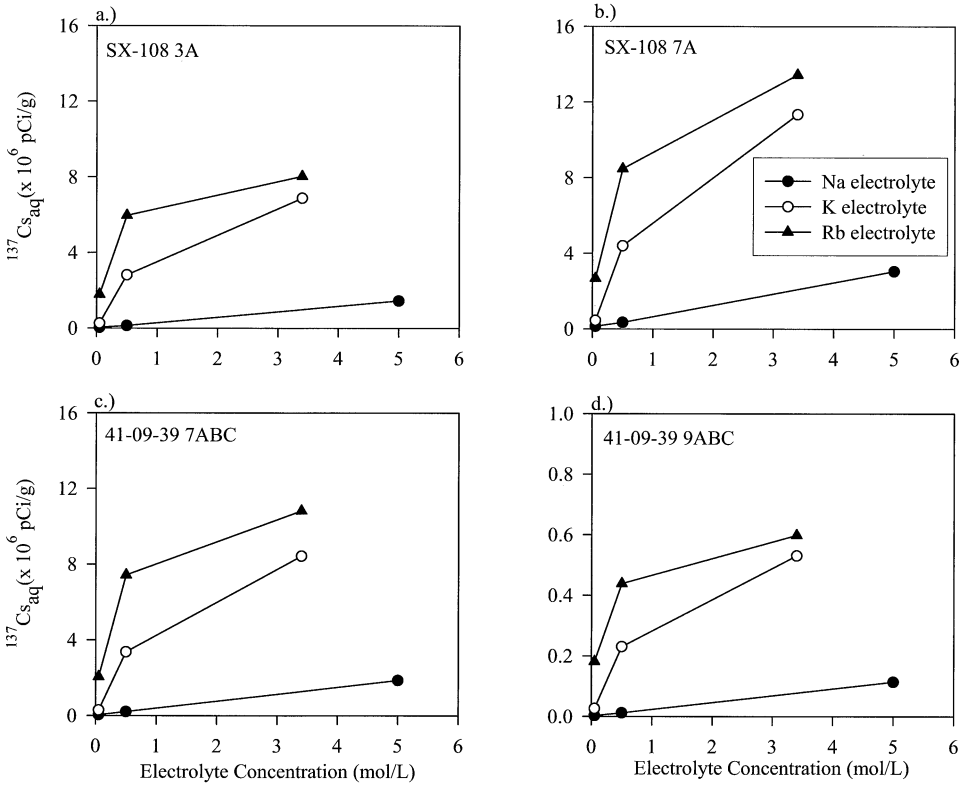

Fig. 2. $^{137}Cs^+$ desorption from the $^{137}Cs^+$-contaminated Hanford sediments below the SX tank farm after 6 d of equilibration as a function of exchanging cations and their concentrations, and sample locations.

again by kinetic desorption. The results indicated that there were at least two pools of $^{137}Cs^+$ in the sediments: an equilibrium exchangeable fraction that was immediately responsive to mass action and a mass transfer limited pool. $^{137}Cs^+$ desorption from the mass transfer limited pool was slow and continued beyond 67 d of equilibration.

The initial release of $^{137}Cs^+$ was generally higher in Rb^+ than K^+ electrolyte, reflecting the stronger selectivity of the sediment exchanger phase for Rb^+ (Table 2). The second stage of $^{137}Cs^+$ desorption, when the electrolyte concentration was increased to 2.0 mol/L, was smaller in Rb^+ electrolyte, suggesting depletion of the exchangeable pool, or possibly edge/interlayer collapse that changed the effective ratio of the exchangeable and mass transfer limited pools. The parallel time dependent behavior in both Rb^+ and K^+ electrolytes indicated that their rates of kinetic desorption were similar. The D_r value was 0.23–0.31 in K^+ and 0.19–0.33 in Rb^+ electrolyte. These ratios were comparable to those calculated for the mass action experiments (Table 3).

Table 3. The percentage of $^{137}Cs^+$ desorbed in Na^+, K^+, and Rb^+ nitrate after contact for 6 days.

	Relative to total initial $^{137}Cs^+$ on the sediments								
	$NaNO_3$			KNO_3			$RbNO_3$		
Concentration (mol/L)	0.05	0.5	.5	0.05	0.5	3.4	0.05	0.5	3.4
SX-108 3A	0.10	0.38	4.22	0.76	8.23	20.1	5.20	17.4	23.5
SX-108 7A	0.23	0.58	5.12	0.74	7.40	19.1	4.50	14.3	24.3
41-09-39 7ABC	0.10	0.52	4.66	0.71	8.39	21.0	5.11	18.5	27.0
41-09-39 9ABC	0.12	0.54	5.18	1.17	10.5	24.2	8.25	20.0	27.2
	Relative to the calculated equilibrium state								
	$NaNO_3$			KNO_3			$RbNO_3$		
Concentration (mol/L)	0.05	0.5	5	0.05	0.5	3.4	0.05	0.5	3.4
SX-108 3A	18.5	22.1	30.3	11.9	18.2	24.5	13.8	20.3	24.0
SX-108 7A	15.8	22.3	43.1	11.2	19.8	25.3	14.4	20.6	23.4
41-09-39 7ABC	16.1	26.0	40.6	13.4	21.2	26.7	16.9	22.4	27.8
41-09-39 9ABC	44.7	35.6	56.4	24.6	24.0	29.8	28.5	23.1	27.9

Table 4. Solutes released from S-SX sediment (in μmol/g) in acid ammonium oxalate (AAO).

Element	SX-108-3A	SX-108-7A	41-09-39-7ABC	41-09-39-9ABC
Al[a]	207.3	211.4	145.1	145.5
Ba[a]	0.2627	0.3162	0.2858	0.1569
Ca[a]	0.1366	0.1339	0.1276	0.1252
Cr[a]	2.480	14.76	32.21	2.249
Fe[a]	420.2	304.5	433.1	334.9
K[a]	16.26	18.16	14.91	13.43
K[b]	7.534	5.333	7.211	4.786
Mg[a]	62.66	67.69	67.14	57.81
Na[a]	62.16	807.9	180.5	46.61
Na[b]	47.53	816.6	156.3	31.92
Si[a]	32.77	33.74	30.90	33.19

[a] Solute released to 0.25 mol/L $(NH_4)_2$-oxalate (pH 3.0) electrolyte after 134 days contact with the sediments.
[b] Na^+ and K^+ released after 2 hours of contact with $(NH_4)_2$-oxalate (pH 3.0) and their concentrations were assumed to be ion exchangeable.

3.5. Sorbent-Induced Cs^+ Desorption

It is possible that high concentration K^+, NH_4^+, and Rb^+ electrolytes may induce collapse of "frayed-edge sites" (FES) where high affinity Cs^+ exchange is believed to occur (Sawhney, 1972). These particular electrolytes were used to induce Cs^+ desorption because their large ion exchange selectivities (Table 2) promote high mass-action pressure. However, electrolyte-induced edge collapse may reduce the apparent "exchangeable fraction" of the sorbed Cs^+ pool. Such a phenomenon may lead to the appearance of poor Cs^+ desorbability or even fixation, artifactual conclusions related to the electrolyte composition. We suspected that such an effect may have limited the mass action response of $^{137}Cs^+$ desorption in Rb^+ electrolyte (2 mol/L; Fig. 3). The exchangeable fraction of sorbed Cs^+ may be higher in electrolytes more representative of field pore water that do not promote collapse of high charge-density phyllosilicate lamellae.

We utilized a highly selective Cs^+ sorbent (SAMMS) in Na^+ electrolyte to evaluate the issue of FES-collapse. The SAMMS is a nanocomposite, mesoporous, high surface area material containing immobilized copper ferrocyanide groups with high selectivity for Cs^+ in Na^+ electrolyte (Lin et al.,

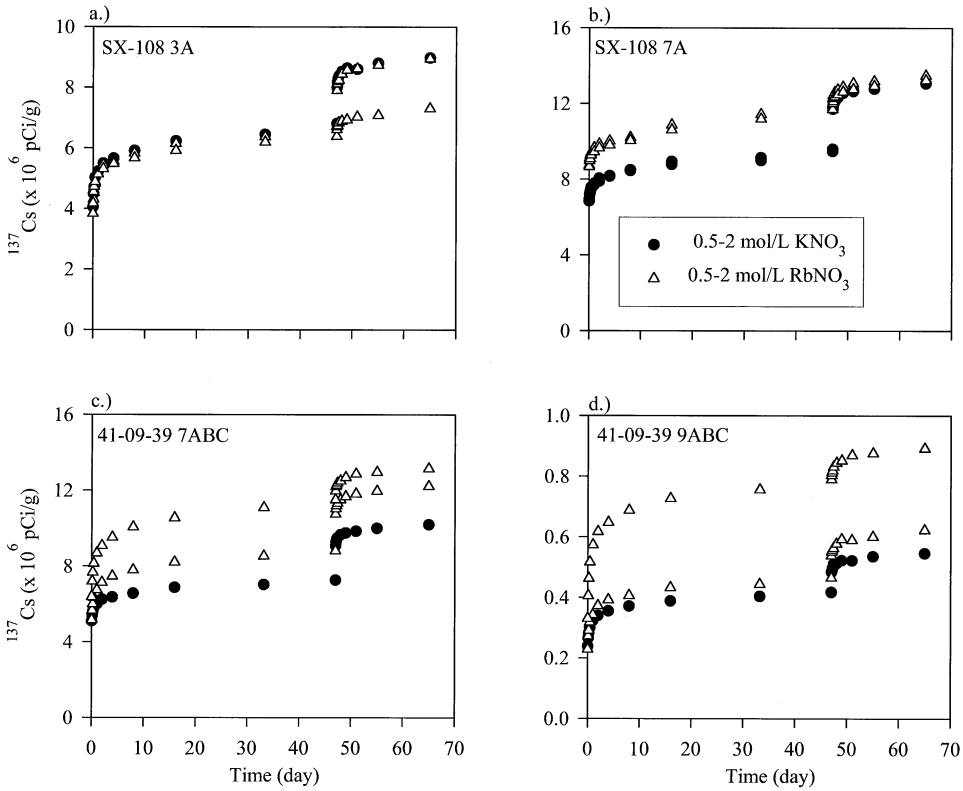

Fig. 3. $^{137}Cs^+$ desorption kinetics from the $^{137}Cs^+$-contaminated Hanford sediments below the SX tank farm in 0.5–2.0 mol/L KNO_3 and $RbNO_3$ electrolytes.

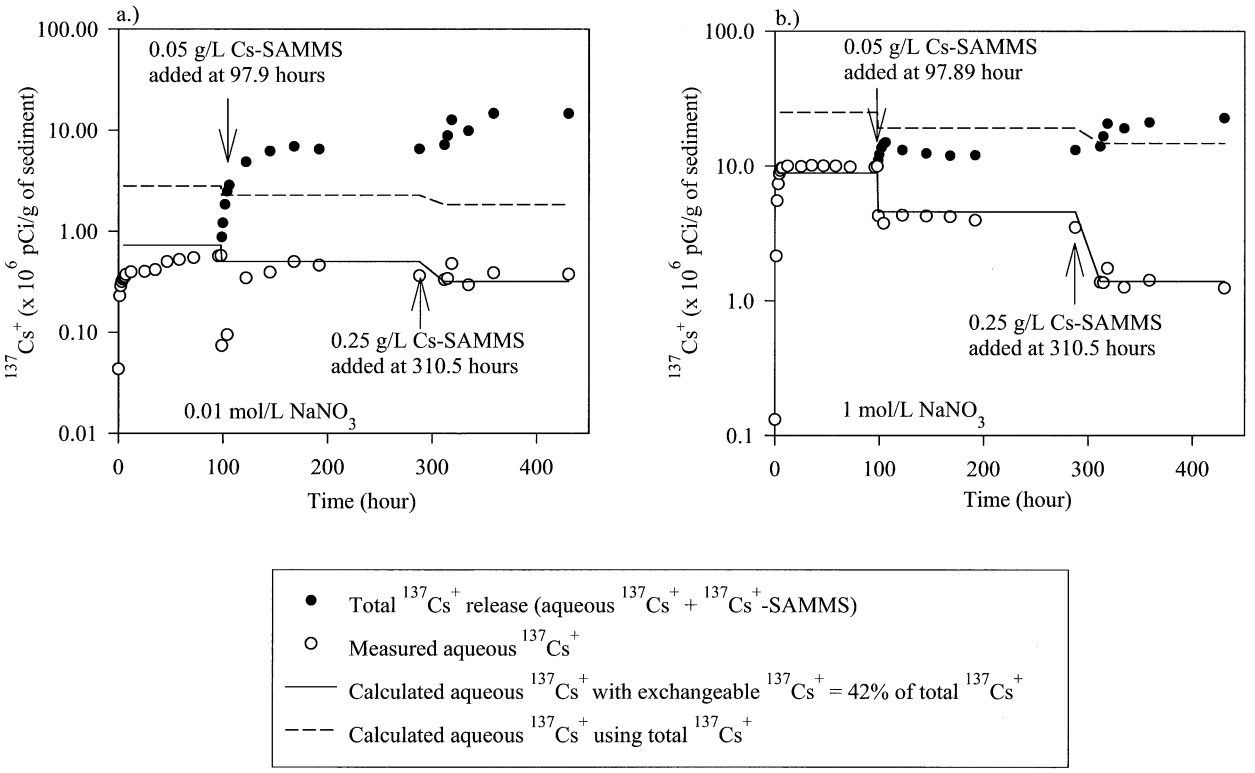

Fig. 4. $^{137}Cs^+$ desorption kinetics from the $^{137}Cs^+$-contaminated Hanford sediments below the SX tank farm in the 0.01 mol/L (Fig. 6a) and 1 mol/L (Fig. 6b) $NaNO_3$ with/without SAMMS. The SAMMS concentrations were increased from zero to 0.05 g/L at 97.9 h, and to 0.25 g/L at 310.5 h.

2001). Sodium nitrate electrolytes of two concentrations (1.0 and 0.01 mol/L) were used that fall within the range of those found in pore waters at this site (Serne et al., 2001a,b). The exchanger phases in the contaminated sediment column are primarily Na^+-saturated from HLW release.

The addition of the competitive sorbent (SAMMS) significantly increased the total desorption of $^{137}Cs^+$ over that observed in $NaNO_3$ electrolyte alone (Fig. 4 compared with Fig. 2b). At low Na^+-concentration (0.01 mol/L $NaNO_3$, Fig. 4a), the first addition of SAMMS (at 100 h) significantly increased the desorption of $^{137}Cs^+_{(tot)}$, which was accompanied by a large decrease in $^{137}Cs^+$aqueous concentration. This behavior reflected the rapid adsorption of $^{137}Cs^+$ by the SAMMS and the slower release rate from the dialysis bag containing sediment. However, the $^{137}Cs^+_{(aq)}$ quickly rebounded to its original concentration even though the Cs^+ site occupation on the SAMMS was only 0.038% [calculated based on 1.35 mmol Cs^+ sites/g of SAMMS, (Lin et al., 2001)]. A five-fold increase in the SAMMS concentration (at 310 h) doubled the Cs^+ desorption (Fig. 4a), with a slight decease in $^{137}Cs^+_{(aq)}$.The total amount of desorbed $^{137}Cs^+$ at experiment termination (430 h) represented approximately 25% of the total sorbed $^{137}Cs^+$in the sample.

The behavior of the SAMMS/sediment system was somewhat different in the higher Na^+ electrolyte (1 mol/L, Fig. 4b). First, the initial $^{137}Cs^+_{(aq)}$ before SAMMS addition was over an order of magnitude higher than in the lower concentration electrolyte because of the mass action effects of Na^+. Second, SAMMS addition promoted small increases in the total desorbed $^{137}Cs^+$concentration, but large decreases in $^{137}Cs^+_{(aq)}$. At experiment termination, approximately the same amount of $^{137}Cs^+$was desorbed in the low and high Na^+ experiments.

The concentrations of $^{137}Cs^+_{(aq)}$ rapidly rebounded to apparent steady state conditions after each episode of SAMMS addition in each electrolyte, indicating approximate adherence to a ternary equilibrium state (e.g., solid-liquid-solid). We calculated the expected concentration of $^{137}Cs^+_{(aq)}$ using our two-site equilibrium ion exchange model (selectivity coefficients in Table 2) after subtracting the $^{137}Cs^+$ mass sorbed on the SAMMS from the sediment pool and assuming that the residual sediment-sorbed $^{137}Cs^+$ was fully exchangeable. These calculations (shown by dashed line in Fig. 4) were higher than the observed concentrations by 0.3–0.6 log units. An excellent agreement with the experimentally observed steady-state $^{137}Cs^+_{(aq)}$ concentrations in both electrolytes was obtained with the assumption that 42% of the $^{137}Cs^+$ pool was exchangeable (Fig. 4, solid lines).

The selectivity coefficients (e.g., log K_v) of the SAMMS for Cs^+-Na^+ exchange were calculated to be 3.37–3.55 in 0.01 mol/L and 4.59–4.67 in 1 mol/L $NaNO_3$ based on the measured $^{137}Cs^+_{(aq)}$ concentration and the computed mole fraction occupation of Cs^+ on the SAMMS. A homogeneous site energy was assumed for the ferrocyanide functional group within SAMMS. The selectivity coefficients of the SAMMS were higher than the low affinity Cs^+ exchange site in the sediment, but over 2 orders of the magnitude lower than high affinity

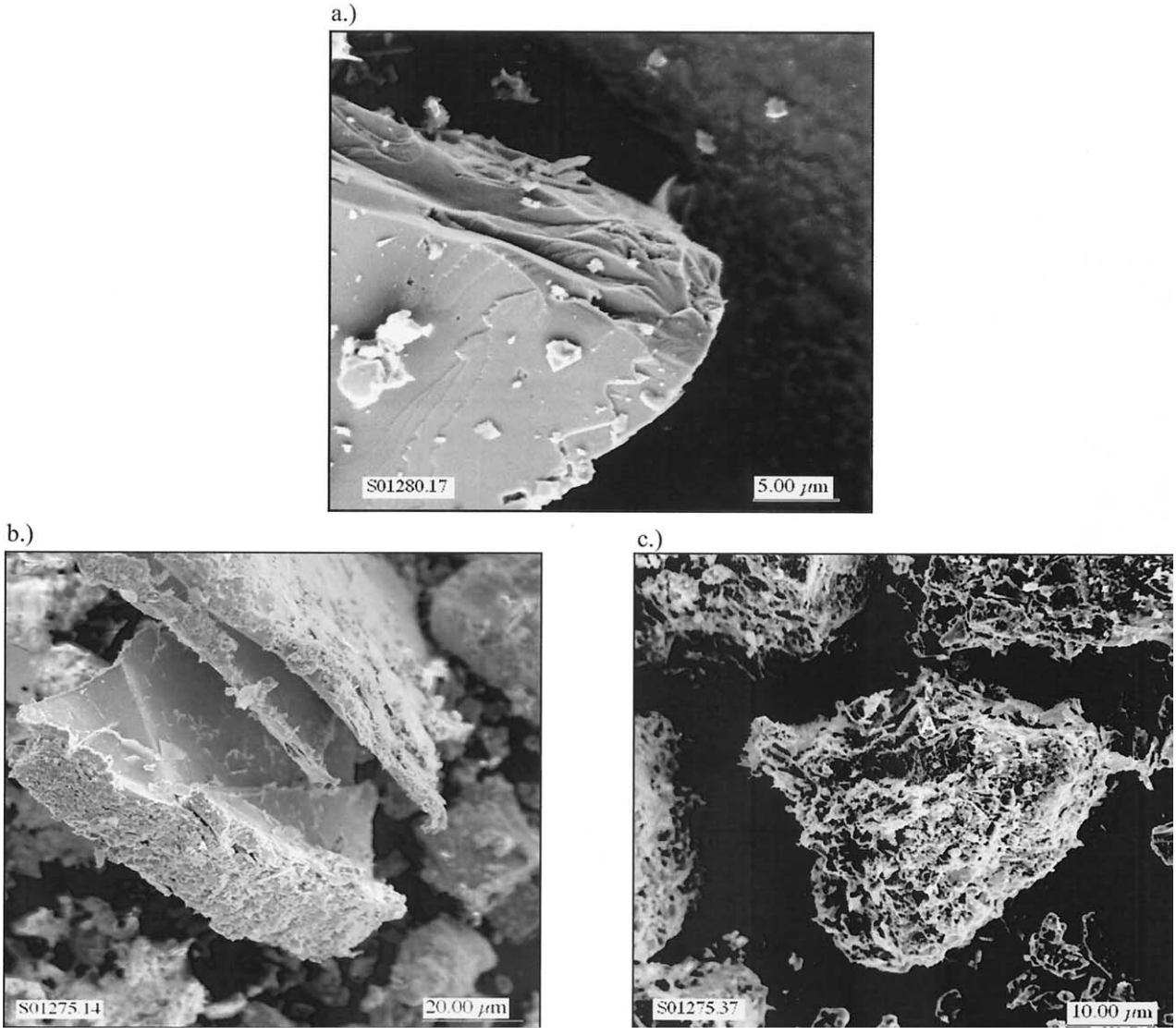

Fig. 5. Scanning electron micrographs of micas isolated from contaminated SX sediment: (a) pristine mica from deep in the sediment column [SX-108, 28.3 m below ground surface (bgs)]; (b) weakly weathered mica with aluminosilicate precipitates on the edges (sample SX-108 7A, 25.8 m bgs); (c) highly weathered mica with copious secondary mineralization (sample SX-108 3A, 20.6 m bgs).

sediment site (Table 2). In spite of its lower selectivity coefficients, the SAMMS was able to displace approximately 60–90% of the computed exchangeable fraction (42%) because of a sizable sorption site concentration of the SAMMS.

3.6. $^{137}Cs^{+}$ Desorption Kinetics in Ammonium Nitrate and Acidified Ammonium Oxalate

We suspected that poorly crystalline materials may have precipitated subsequent to Cs^{+} adsorption through waste-sediment reaction (the waste stream was high in OH^{-} and $Al(OH)_4^{-}$), and that these secondary phases might effectively armor the surface and block Cs^{+} desorption. Indeed, micas isolated from the contaminated sediment showed evidence for such precipitates. Micas from deep in the contaminated sediment column (28.3 m, Fig. 5a) were clean and identical in appearance to those isolated from pristine sediment. At intermediate depths (25.8 m, SX-108 sample 7A; Fig. 5b) micas retained their original tabular morphology, but showed the presence of surface coatings of fibrous, secondary precipitates. Severe particle alteration was noted in samples collected proximate to the HLW waste source (20.6 m, SX-108 sample 3A; Fig. 5c) where micas were completely encrusted with secondary phases and particle morphology was indistinct. Energy dispersive spectroscopy (EDS) analysis of these precipitates showed the presence of Na, Al, Si, and Fe in variable concentration.

Acidified ammonium oxalate (AAO) dissolves poorly crystalline Al and Fe oxides (Loeppert and Inskeep, 1996), and was used here to remove these phases while simultaneously applying mass action pressure (via the ammonium ion) to desorb $^{137}Cs^{+}$. Ammonium nitrate, in turn, was used as a control to

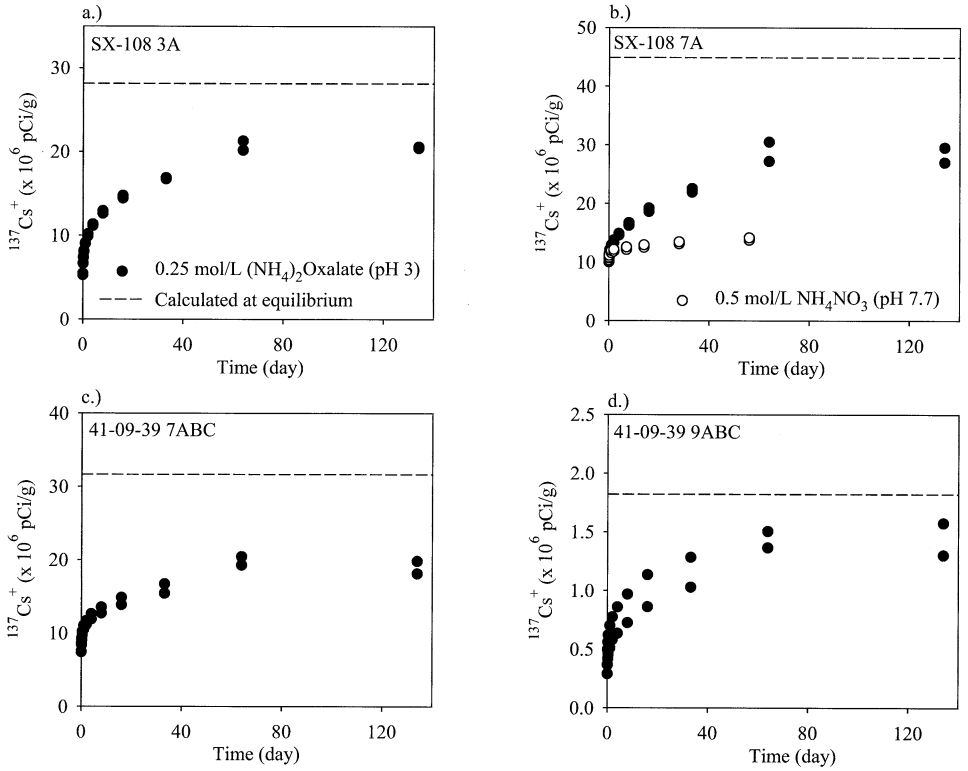

Fig. 6. $^{137}Cs^+$ desorption kinetics from the $^{137}Cs^+$-contaminated Hanford sediments below the SX tank farm in 0.5 mol/L NH_4NO_3 and 0.25 mol/L $(NH_4)_2$-oxalate (pH 3). The dashed lines were $^{137}Cs^+$ desorption in 0.5 mol/L NH_4^+ calculated for each sediment at equilibrium using the two-site ion exchange model with measured total Cs^+ concentration and CEC (Table 1), and the estimated selectivity coefficients (Table 2).

evaluate the extraction potential of the NH_4^+ ion in the absence of proton-promoted dissolution. The kinetic behavior of $^{137}Cs^+$ desorption in NH_4NO_3 (0.5 mol/L) (Fig. 6b) was similar to that observed in K^+ and Rb^+ electrolytes (e.g., Fig. 3b). Although the same quantity of $^{137}Cs^+$ was desorbed by NH_4NO_3 and AAO in the initial exchange event, the latter extractant significantly enhanced the long-term desorption rate and extent (Fig. 6b). Sample 9ABC, again, showed the worst reproducibility because of its relatively coarse texture. $^{137}Cs^+$ desorption in AAO continued for ~65 d and then ceased. In contrast, Cs^+ desorption in K^+ and Rb^+ nitrate electrolytes extended over the experimental duration (>70 d) (Fig. 3), albeit at a slow rate. Measurements of suspension pH at the termination of AAO experiment averaged 3.25, indicating significant remaining acidity and extraction potential. The desorbed $^{137}Cs^+$ concentrations after 63 d in AAO were averaged for each sediment and were found to represent 63, 46, 46, and 64% of total $^{137}Cs^+$, and 77, 61, 62, and 78% of the calculated $^{137}Cs^+$ desorption at exchange equilibrium for sediments 3A, 7A, 7ABC, and 9ABC, respectively.

Acidified ammonium oxalate dissolves poorly crystalline Fe(III)/Al(III) oxides without significant change to coassociated layer silicates if limited to contact times of approximately 2 h (Loeppert and Inskeep, 1996). Significant Fe, Al, and Si were extracted in the first 2 h (first data point, Fig. 7), consistent with the presence of poorly crystalline Fe(III) and/or Al(III) oxides. All of the sediments released comparable quantities of Al and Fe in spite of gross differences in their physical appearances (Fig. 5). The removal of these materials did not significantly increase the initial desorption of $^{137}Cs^+$ as shown in Figure 6b (e.g., the same initial concentration of $^{137}Cs^+$ was desorbed from sample 7A in both NH_4NO_3 and AAO). With time, the concentrations of dissolved Al, Fe, and K continued to increase in almost parallel manner (Fig. 7), consistent with the dissolution of iron-containing expansible [Fe(III)-biedellite] and nonexpansible (biotite, clinochlore) layer silicates known to exist in these sediments. The release profiles of these elements, in turn, paralleled the long-term desorption profiles for $^{137}Cs^+$ (Fig. 6), suggesting $^{137}Cs^+$ release by dissolution of more soluble phases or structural regions (e.g., frayed edges) in the layer silicate fraction.

3.7. Kinetics of Cs^+ Adsorption/Desorption on Pristine Sediment

The kinetics of Cs^+ adsorption and desorption on the pristine "Above B" sediment were examined to investigate mass transfer and edge collapse phenomena believed to be important in the desorption behavior from contaminated sediment. The pristine sediment allowed characterization of the short-term adsorption/desorption process in the absence of HLW-induced secondary mineral precipitation.

Cesium sorption to the "Above B" sediment reached an equilibrium state ($D_r = 1$) in less than 10 d in 0.1 mol/L $NaNO_3$

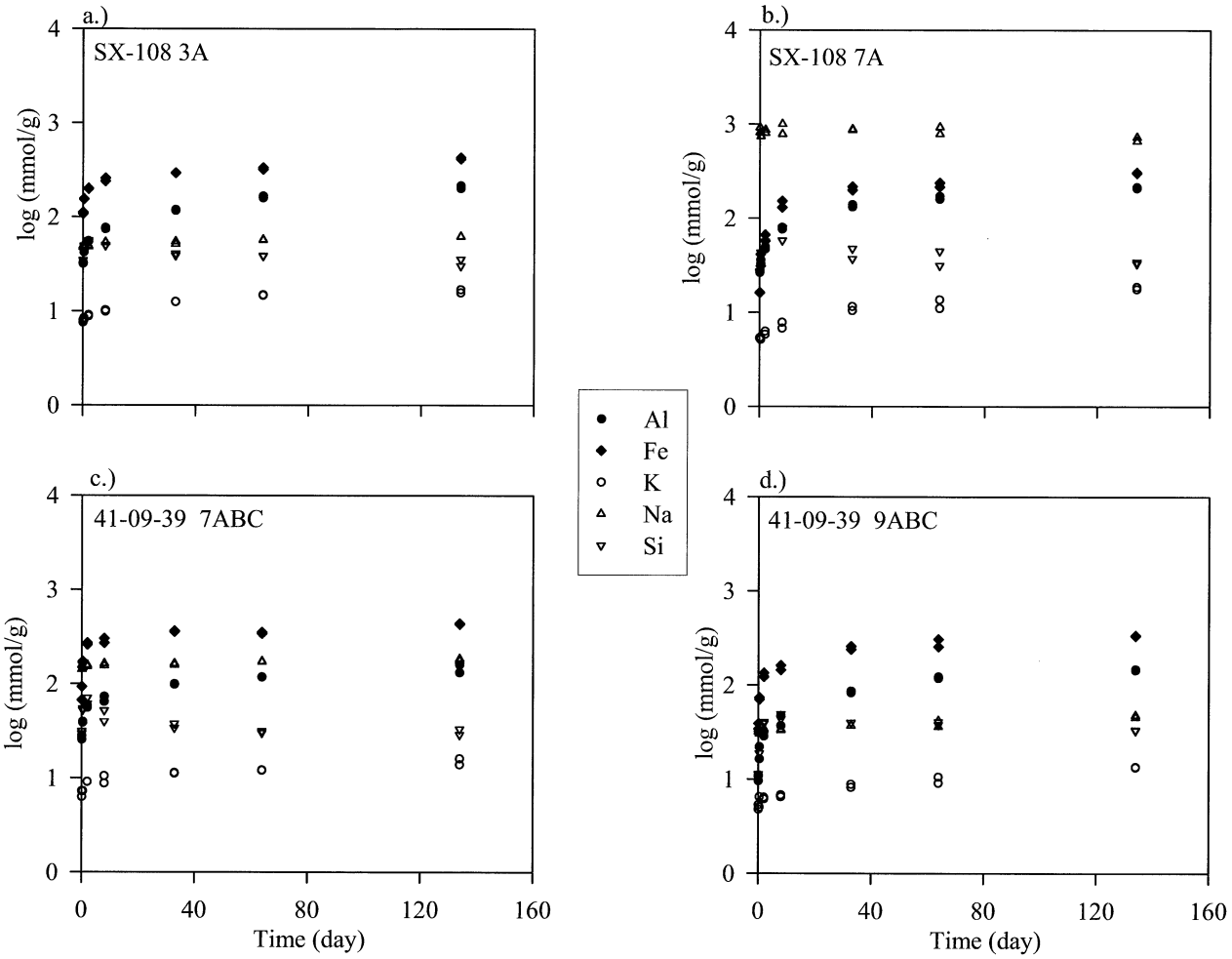

Fig. 7. Solute concentrations accompanying $^{137}Cs^+$ desorption from the $^{137}Cs^+$-contaminated Hanford sediments below the SX tank farm in 0.25 mol/L $(NH_4)_2$-oxalate (pH 3) (Fig. 3).

(Fig. 8a). The adsorption reaction after 1 d contact was reversible, with desorption reaching equilibrium (e.g., $D_r = 1$) in less than 10 d after 50-fold increase in $NaNO_3$ concentration to 4.9 mol/L (Fig. 8b). Cesium that had been adsorbed for 27 d and 70 d in 0.1 mol/L $NaNO_3$ desorbed to the equilibrium state in 24 h in 4.9 mol/L $NaNO_3$ (Fig. 8c). These results contrasted with the contaminated sediments that displayed $D_r = 0.30–0.56$ after 6 d

In contrast, desorption extent in Rb^+ and K^+ electrolyte was well below the computed equilibrium state regardless of aging time of the sorption complex or desorption period (Figs. 8b,c). The D_r value was lowest for Rb^+, which exhibited the highest mass action pressure given its large selectivity coefficient (Table 2). Desorption was both limited and slow in K^+ and Rb^+ electrolyte after only 1 d of sorptive contact (Fig. 8b). The increase in desorption with time suggested mass transfer limitations. Also suggestive of mass transfer to intraparticle regions was the decrease in 1-d desorbability in K^+ and Rb^+ electrolytes that accompanied aging time of the sorption complex (Fig. 8c). The D_r value ranged from 0.4 to 0.6 for the pristine sediment after short-term Cs^+ contact as compared to 0.23 to 0.30 after long-term contact in the contaminated sediments (Table 3).

XRM measurements of the spatial distribution of adsorbed Cs^+ in mica taken from the pristine sediment after 28 d of contact with 10^{-3} mol/L $CsNO_3$ showed distinct sorptive localization at specific areas on the mica edge (Fig. 9), consistent with the frayed-edge site model of Cs^+ adsorption (Zachara et al., 2002, and references therein). These micas are the primary radiocesium sorbents in the contaminated sediment (McKinley et al., 2001). Also evident was sorbed Cs^+ in intraparticle channels parallel to the mica basal plane. The intraparticle distances (20–50 μm) are many orders of magnitude beyond the scale attributable to solid-state diffusion. The channels are likely representative of cleavage faces and/or exfoliating mica lamellae. Results (Fig. 9) are shown for muscovite, but analogous findings were observed for biotite (McKinley et al., 2001), which is the more significant radiocesium sorbent (McKinley et al., 2001). These images provide a visual conceptual model of different domains in which mass transfer may be an important control on desorption rate and extent. These include frayed regions on the mica edge susceptible to complex electrolyte-

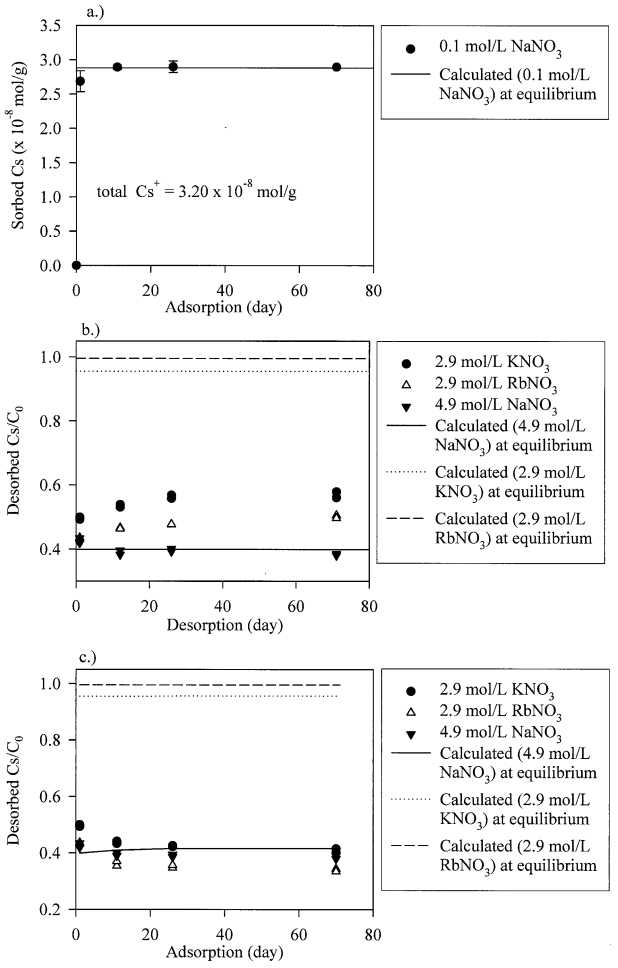

Fig. 8. Cs^+ adsorption and desorption on pristine Hanford sediment: showing (a) Cs^+ adsorption kinetics in 0.1 mol/L $NaNO_3$; (b) Cs^+ desorption kinetics in 4.9 mol/L $NaNO_3$ and 2.9 mol/L KNO_3 or $RbNO_3$ from Cs^+-loaded sediments after 1 d of Cs^+ adsorption in 0.1 mol/L $NaNO_3$); (c) Cs^+ desorption after 1 d of equilibration in 4.9 mol/L $NaNO_3$ and 2.9 mol/L KNO_3 or $RbNO_3$ from Cs^+-loaded sediments (after variable days of adsorption in 0.1 mol/L $NaNO_3$). The lines were equilibrium concentrations calculated using the two-site ion exchange model.

induced swelling and collapse, and deep intraparticle regions existing along cleavage planes with contact to the aqueous phase. We suggest that this conceptual model applies to micas in the contaminated sediment with the additional complication of the secondary surface precipitates as shown in Figure 5.

4. DISCUSSION

4.1. Desorption Process

Cesium desorption from the contaminated sediment was a nonequilibrium process characterized by two distinct stages: a rapid initial release followed by a slow kinetic one. The first stage was consistent with ion exchange displacement of Cs^+ from fixed charge sites in close communication with the aqueous phase. Observations that, i.) the rapid Cs^+ desorption increase with exchanging cation concentration (Figs. 2 and 3), and ii.) the total amount of Cs^+ desorption paralleled the selectivity trend of the electrolyte cations: $Rb^+ > K^+ > Na^+$ (Fig. 2, Table 3), support this posit. Only a fraction of the adsorbed Cs^+ was initially exchangeable (e.g., Table 3, Fig. 6), however, and this fraction showed complex dependence on various factors. Application of the two-site ion exchange model (Zachara et al., 2002; Liu et al., 2003) inferred that 10–55% of the total Cs^+ was exchangeable depending on the type and concentration of the exchangeable cation and the specific sediment sample. There was no apparent dependence of exchangeability on Cs^+ adsorption density (e.g., compare 7A and 9ABC in Figs. 2 and 3 and Tables 1 and 3).

The ratio of the total adsorbed Cs^+ to high affinity exchange sites was < 0.7 in all the sediments (Table 1), suggesting localization of sorbed Cs^+ to high affinity exchange sites. Previous work (Zachara et al., 2002) suggests that the high affinity sites reside primarily on weathered mica edges (e.g., Fig. 9), where unique, stereo-selective wedge sites developed (Le Roux et al., 1970). Consistent with this, sorbed radiocesium was observed to associate primarily with micas of different types in these sediments (McKinley et al., 2001). Some spillover of adsorbed Cs^+ to low affinity sites may have occurred in the contaminated sediments depending on K^+ adsorption density, but this value is not known with certainty. Given this caveat, our results imply that a significant fraction of the Cs^+ adsorbed to the high affinity sites was rapidly exchangeable.

The second, kinetic stage has been attributed to Cs^+ diffusion from recessed, high affinity edge-interlayer adsorption sites (Comans and Hockley, 1992). The XMP image of Cs^+-sorbed muscovite from pristine Hanford sediment (Fig. 9) represents one example of the spatial regions where these sites may reside. The short-term kinetic studies with the pristine sediment provided insights on the relative rates of diffusion from these domains in Hanford sediment and the profound impact of electrolyte cation. The desorption (e.g., diffusion) rate was fast in $NaNO_3$, but decreased when Cs^+-sorbed, pristine sediment from $NaNO_3$ electrolyte was placed in high concentration K^+ and Rb^+ electrolytes (Figs. 8b,c). Implied was rapid edge-interlayer collapse resulting from saturation of the exchange complex with K^+ and Rb^+ (Sawhney, 1967, 1969, 1972; Eberl, 1980; Comans et al., 1991). The collapse decreased the amount of adsorbed Cs^+ that was displaceable by mass action, and as well as the desorption/diffusion rate. Applying our two-site ion exchange model allowed us to conclude that approximately 50% of the adsorbed Cs^+ was rendered nonexchangeable in 2.9 mol/L K^+ and Rb^+ electrolyte. More collapse was implied in Rb^+ electrolyte (Fig. 8), consistent with its lower hydration energy. Collapse was also implied in the desorption experiments with contaminated sediments by the smaller incremental release that occurred when the Rb^+ concentrations exceeded 1 mol/L (Figs. 2 and 3).

First order rate constants were fit to the concentration data in Figure 3 and Figure 8 after the initial release events to allow comparisons of desorption rates with other published values.The rate constants for Cs^+ desorption was $\sim 10^{-3}$ d^{-1} (half-life of $\sim$700 d) from both pristine (after 1 d aging of the sorption complex, Fig. 8b) and the contaminated sediment (first desorption period in Fig. 3). Equivalent first order rate constants for Cs^+ diffusion into illite intraparticle regions in K^+ electrolyte were also in the order of 10^{-3} d^{-1}

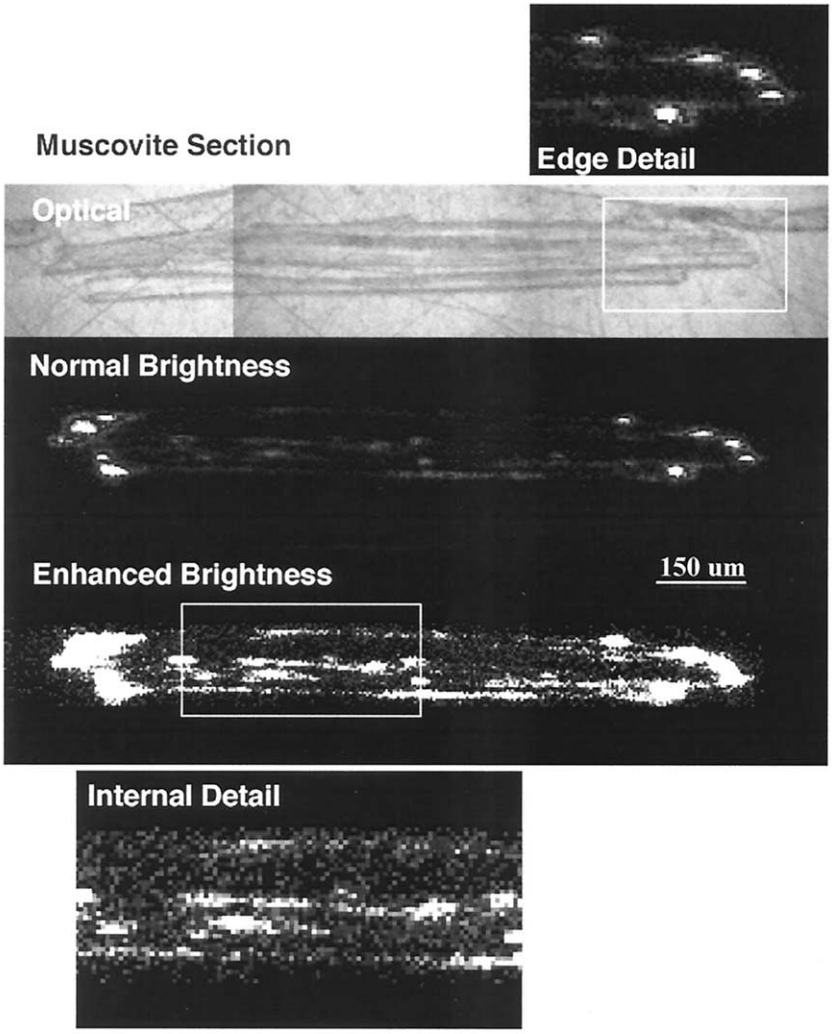

Fig. 9. X-ray microprobe images of Cs^+-loaded muscovite flake: showing the $^{137}Cs^+$ distribution on edges and also intraparticle channels parallel to the mica basal plane.

(Comans and Hockley, 1992). In contrast, the estimated rate constant for pristine Hanford sediment in $NaNO_3$ was 0.3 d^{-1} (half-life of 2.3 d), which underscored the rapid and unique desorption behavior for Cs^+ in that specific experimental system.

The apparent exchangeability and long-term kinetic release rates of sorbed Cs^+ were different in the pristine and contaminated sediments. We originally believed that this difference could result from the presence of the secondary precipitates that so obviously coated mineral grains in the contaminated samples (Figs. 5b,c). Such precipitates might veneer the surfaces, preventing water or electrolyte exchange. Desorption experiments were performed in AAO to evaluate such effects. The results of these experiments showed no difference in the rapidly exchangeable fraction after 2 h of extraction (e.g., Fig. 6b), the time period deemed appropriate for removal of poorly crystalline oxides. Thus, the secondary precipitates did not appear to influence the exchangeable fraction of adsorbed Cs^+ and/or the amount of Cs^+ release in the first stage of desorption. However the rate and extent of the long-term desorption process was markedly increased by continued contact with AAO. Exposure to AAO in excess of 2 h can promote layer silicate dissolution, and the continued increase in supernatant K^+ and Al^{3+} implied such reaction. The enhanced long-term release may be attributed to two factors: i) the removal of surface coatings relieved mass-transport impediments at the mica-water interface allowing for greater diffusive flux from internal channels and pore spaces, or ii) time-variant dissolution of high surface area mica edge regions released sorbed Cs^+ from collapsed high-affinity site domains. Although our study cannot discriminate between these two mechanisms, we feel the latter explanation is supported by the approximately parallel rates of evolution of K^+, Al^{3+}, and Cs^+ from 1 to 70 d.

4.2. Modeling Nonequilibrium Desorption

Nonequilibrium Cs^+ ion exchange has been modeled using coupled sequences of kinetic steps (Liu et al., 1994), and coupled equilibrium exchange with a first-order approximation to the diffusive process (Comans and Hockley, 1992). The former approach assumed that Cs^+ ion exchange consisted of 3

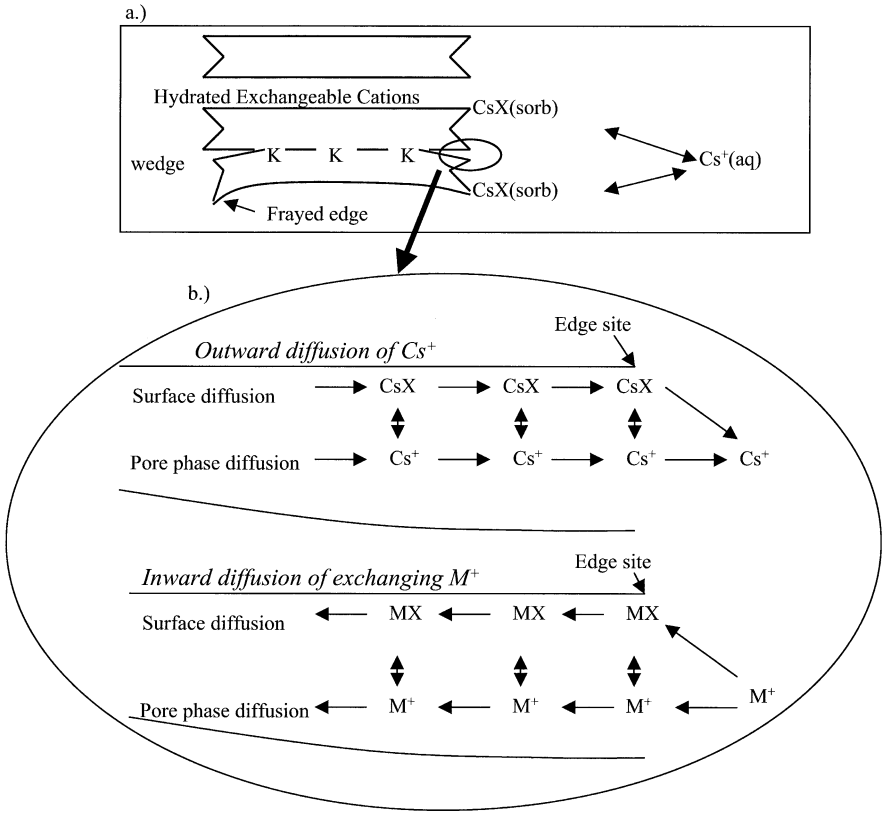

Fig. 10. Schematic diagram of Cs exchange between external edge sites and aqueous phase (Fig. 10a), and diffusion and exchange within the edge-interlayer regions (Fig. 10b).

different kinetic steps: i) film diffusion between the aqueous and solid phase, ii) a kinetic sorption reaction at the surface, and iii) intraparticle diffusion from external to internal adsorption sites. Differential site energetics was not considered and the individual kinetic steps required discrete characterization (Sposito, 1994), which was found to be difficult. The second approach separated exchange sites into two or three boxes (Comans and Hockley, 1992). In the two-box model, ion exchange was assumed to be kinetic; ion exchange in the first box was reversible and connected to the second box, where ion exchange was allowed slow reversibility (months and years) (Cowan et al., 1991). The three-box model consisted of the two-box model, supplemented by an additional box where ion exchange was in equilibrium with the aqueous phase. The kinetic processes in both the two-box and three-box models were approximated by first-order models and equilibrium exchange was modeled using the Freundlich isotherm.

The experimental observation of a two stage desorption process (Figs. 3 and 8) combined with Cs^+ sorptive localization at specific edge regions and internal channels (Fig. 9) lead us to propose the descriptive model in Figure 10. The model includes equilibrium ion exchange on external surface sites (Fig. 10a) and counter-current Cs^+-M^+ (exchanging cation) diffusion into/from edge-interlayer regions. A slab diffusion model was assumed because of the layer characteristics of $^{137}Cs^+$ distribution on the edge and within the intraparticle region (Fig. 9). For ease of discussion, the edge-interlayer sites exhibiting kinetic or diffusion-limited sorption are considered intraparticle sites. The model for intraparticle sites was described as follows:

Cs^+ diffusion:

$$\frac{\partial q_{Cs}}{\partial t} = D_p^{Cs}\frac{\partial}{\partial x}\left(\varepsilon_p(x)\frac{\partial [Cs^+]_{aq}^{in}}{\partial x}\right) + \rho_s D_s^{Cs}\frac{\partial}{\partial x}\left((1-\varepsilon_p(x))\varphi(x)\frac{\partial [CsX]^{in}}{\partial x}\right) \quad (8)$$

Exchanging cation diffusion:

$$\frac{\partial q_{M^+}}{\partial t} = \varepsilon_p D_p^M\frac{\partial}{\partial x}\left(\varepsilon_p(x)\frac{\partial [M^+]_{aq}^{in}}{\partial x}\right) + p_s D_s^M\frac{\partial}{\partial x}\left((1-\varepsilon_p(x))\varphi(x)\frac{\partial [MX]^{in}}{\partial x}\right) \quad (9)$$

Equilibrium cation exchange on intraparticle sites:

$$[CsX]^{in} = \frac{K_v^{in}\{Cs^+\}_{aq}^{in}\varphi(x)}{\{M^+\}_{aq}^{in} + K_v^{in}\{Cs^+\}_{aq}^{in}} \quad (10)$$

where $[Cs^+]_{aq}^{in}$ and $\{Cs^+\}_{aq}^{in}$, and $[M^+]_{aq}^{in}$ and $\{M^+\}_{aq}^{in}$ are the aqueous concentrations and activities of Cs^+ and exchanging cation M^+ in the intraparticle pores, respectively; q_{Cs+} and q_{M+} are the total concentrations (aqueous + sorbed); D_p^i and

D_s^i are the diffusivities for aqueous and sorbed species i, respectively; $[CsX]^{in}$ and $[MX]^{in}$ are the equivalent fraction of sorbed species of Cs^+ and M^+ on intraparticle sorption sites, respectively; $\varepsilon_p(x)$ is the intraparticle porosity; ρ_s is the solid density; and $\varphi(x)$ is the intraparticle sorption site density.

Eqns. 8–10, when coupled with two-site equilibrium ion exchange on external sites at the aqueous-solid boundary, is a mathematically complete diffusion problem. However, the problem solution requires microscopic information, including the intraparticle porosity, the intraparticle site density, and aqueous and surface diffusivities of both Cs^+ and exchanging cations in the intraparticle regions. These properties are difficult to measure and therefore, the model required simplification to be tractable. Considering that the intraparticle porosity is usually small (Ball and Roberts, 1991) and that Cs^+ strongly adsorbs to edge-interlayer sites (Sawhney, 1967, 1969, 1972; Eberl, 1980), we assumed that the Cs^+ mass associated with the intraparticle aqueous phase was negligible compared to the sorbed phase. With this assumption and considering cases when surface diffusion was the rate-limiting process, the intraparticle problem defined by Eqns. 8–10 was simplified to one equation:

$$\frac{\partial q_{Cs}}{\partial t} \approx \rho_s \varphi(Y) \frac{\partial [CsX]^{in}}{\partial t} = \rho_s (D_s^{Cs}/L^2) \frac{\partial}{\partial Y}\left(\varphi(Y) \frac{\partial [CsX]^{in}}{\partial Y} \right) \tag{11}$$

where y is a dimensionless variable, Y = x/L (diffusion distance x normalized by an average intraparticle diffusion length, L).

Surface diffusion has been proposed as a rate-limiting process in the intraparticle diffusion of Cs^+ in clayey soils (Liu et al., 1994). Rigorous characterization of surface diffusion, however, is rarely achieved because of the difficulty in experimentally distinguishing aqueous and surface diffusion (Cussler, 1995). The assumption that either aqueous or surface diffusion is the rate-limiting process is often used to simplify the mathematical mass transport problem (such as Eqns. 8–10) and to avoid difficult characterization of the individual diffusive processes (Cussler, 1995; Do, 1998). In such cases, the experimentally determined diffusion parameter, such as D_s in Eqn. 11, is an apparent one (Do, 1998), lumping the potential effects of both processes.

In the following analysis, we used Eqn. 11 instead of Eqns. 8–10 to describe Cs^+ diffusion because of its simplicity and minimal number of parameters. The parameters in Eqn. 11 include the lumped effects of both aqueous and surface diffusion in the intraparticle regions as described by Eqns. 8–10. The boundary conditions for Eqn. 11 were formulated as:

$$[CsX]^{in}\Big|_{Y=0} = [CsX]^{eq,HA}(t);\ \frac{\partial [CsX]^{in}}{\partial Y}\Big|_{Y=1} = 0;\ 0 \le t < +\infty \tag{12}$$

where $[CsX]^{eq,HA}(t)$ is the equivalent fraction of sorbed Cs^+ on the equilibrium, high affinity sites presumed to exist on the mica edge. A no mass flux condition was used at the internal end of the intraparticle pore channel. The initial condition was generally taken as:

$$[CsX]^{in}|_{t=0} = f(Y);\ 0 \le Y \le 1 \tag{13}$$

The numerical solution to Eqn. 11 that was constrained by the conditions of Eqn. 12 and 13 was coupled with the equilibrium two-site ion exchange model applied to external sites. The problem was solved by a sequential iteration approach at each time step through the boundary condition at the edge site (Eqn. 12). A fully backward finite difference scheme was used in solving Eqn. 11. The parameter, D_s^{Cs}/L^2, in Eqn. 11 was lumped as a fitting parameter because of the difficulty in determining a unique value for the diffusion length. The intraparticle site density, φ(Y), was assumed to be a hyperbolic function, with higher site density near the solid surface and lower density toward the inside of intraparticle pore channel:

$$\varphi(Y) = \frac{a}{b + Y} \tag{14}$$

The fitting parameters a and b were related by the following constraint:

$$\int_0^1 \varphi(Y)dY = E^{in}CEC \tag{15}$$

where E^{in} is the equivalent fraction of intraparticle sorption sites in term of the total sediment CEC. The intraparticle site density function (Eqn. 14) was not experimentally measured, but may be a function of particle size, interlayer and edge weathering degree, Fe(II/III) content of the mica, the lumped effects of intraparticle pore channels with different length and tortuosity, and other as yet undefined properties. Although the higher site density near the surface was supported by the XRM analyses (bright spots in Fig. 9), the continuous hyperbolic decrease of site density toward particle interior was a mathematical simplification that seemed justifiable.

The diffusion model well described Cs^+ adsorption and desorption behavior on the uncontaminated Hanford sediment in $NaNO_3$ electrolyte (Fig. 11). Three parameters: diffusivity (D_s^{Cs}/L^2), the shape parameter of the site density function (b), and the ratio of external to intraparticle high affinity sites (E^{ext}/E^{in}), were used to simultaneously fit all experimental results in Figure 11. The total CEC (82.5 μEq/g) and the fraction of high affinity sites (4.5×10^{-4}) were fixed at previously determined values (Zachara et al., 2002; Liu et al., 2003). The selectivities of both internal and external sorption sites were assumed to be identical. The assumed hyperbolic site density function was found necessary to simulate the experimental results of Figure 11c. The best-fit parameters (Table 5) implied that: 1) more than half of the high affinity sites were subjected to the kinetic process, 2) internal site density was much higher near the mineral surface and rapidly decreased into the intraparticle region, and 3) diffusion from the intraparticle region was fast in $NaNO_3$ electrolyte.

The fitted parameters from $NaNO_3$ electrolyte, however, significantly over-predicted the Cs^+ desorption in KNO_3 and $RbNO_3$ electrolytes (Fig. 12). Both the diffusion parameter and the ratio of external to intraparticle sites had to be reduced to fit the experimental results (Table 5). The results suggested that

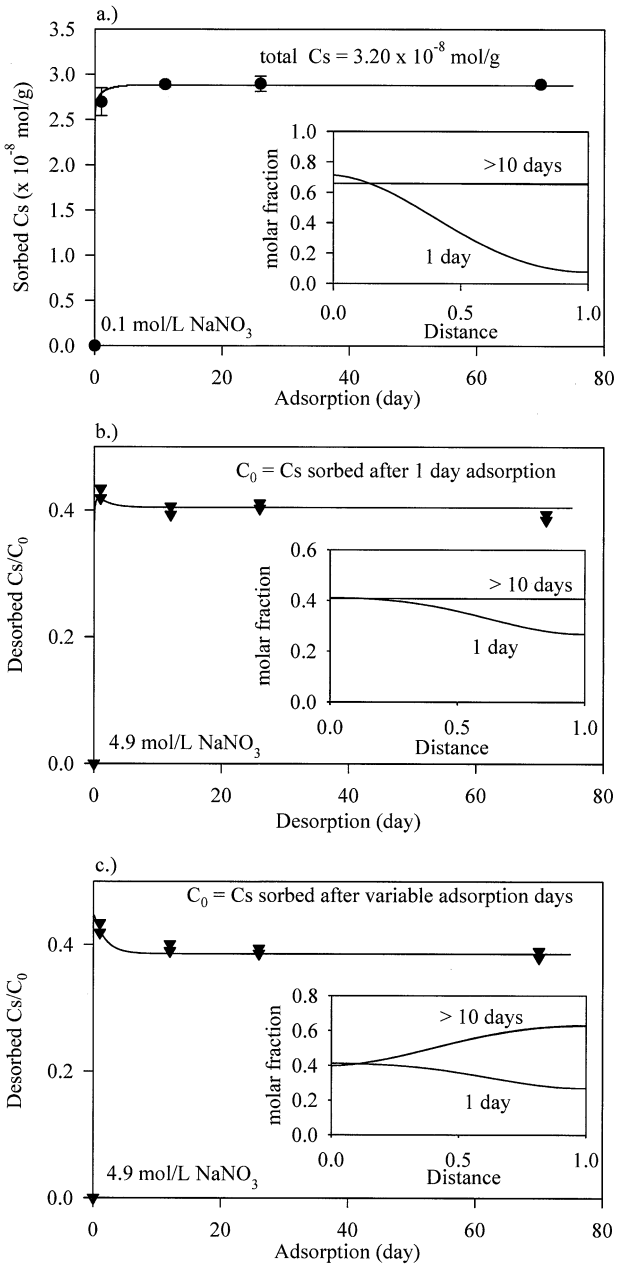

Fig. 11. Results of the coupled model of Cs^+ diffusion within edge-interlayer regions and equilibrium ion exchange on two external sites. (a) Cs^+ adsorption in 0.1 mol/L $NaNO_3$ electrolyte (inset shows the intraparticle distributions as a function of time); (b) time-variant desorption in 4.9 mol/L $NaNO_3$ after 1 d adsorption in 0.1 mol/L $NaNO_3$; (c) results after 1 d desorption in 4.9 mol/L $NaNO_3$ after variable days of adsorption in 0.1 mol/L $NaNO_3$.

interlayer/edge collapse in K^+ and Rb^+ electrolytes reduced i.) Cs^+ diffusivity within the intraparticle region, and ii.) the number of high affinity sites subject to equilibrium ion exchange.

Modeling Cs^+ desorption from the contaminated sediments was complicated by the long exposure time, the unknown intraparticle spatial distribution of radiocesium, the presence of secondary surface precipitates and other HLW-induced weathering effects (e.g., changes of site concentration and high/low affinity site distribution), and edge-interlayer diffusion and collapse in high K^+/Rb^+ electrolyte system. Modeling desorption from the contaminated sediments (Fig. 13), required that the ratio of exchangeable Cs^+ (including equilibrium and kinetic) to the total sorbed Cs^+ on the sediment; and the fraction of high affinity sites also be considered as adjustable parameters. To provide consistency, the diffusion parameters and site density function were kept the same as for the "Above B" sediment in K^+ and Rb^+ electrolytes (Table 5). We also assumed that the ratio of external to intraparticle high affinity sites and the overall fraction of high affinity sites relative to the CEC were the same for all 4 contaminated samples (Table 5). The measured Cs^+-CEC and total Cs^+ concentration for each contaminated sediment (Table 1) were used in the modeling.

The slab diffusion model produced reasonable simulations of the Cs^+ desorption results from the SX-108 sediments (3A and 7A, Fig. 13) in both KNO_3 and $RbNO_3$ electrolytes using the parameters in Table 5. The 41-09-39 samples were not included here because of the large apparent variability in $[Cs^+]_{total}$ between replicates (Figs. 3c,d). According to the model, desorption is described in two stages: i.) rapid ion exchange from external, high energy sites, and ii.) kinetic, diffusion-retarded ion exchange from internal, high affinity sites. Relative to the pristine sediment, an acceptable fit to the desorption data for the contaminated sediments was obtained by: i) increasing the high affinity site fraction (E^{in+ext}) by ~27%, ii) increasing the ratio of external to internal high affinity sites (E^{ext}/E^{in}; e.g., distributing the increased high affinity site concentration to particle exteriors rather than interiors), and iii) decreasing the fraction of sorbed Cs^+ that was exchangeable. The difference in the concentration and distribution of the high affinity sites relative to the pristine sediment was tentatively attributed to the effects of waste-sediment reaction. Unpublished results of the influence of waste-sediment reactions on the Cs^+ sorption to the Hanford site sediment qualitatively support this tenet (Ainsworth et al., personal communication). The nonexchangeable fraction (e.g., 63–55%) was the sorbed Cs^+ pool that did not contribute to desorption over the time period of the experiment (e.g., 60 d). This pool is effectively fixed by the solid phase.

A common set of parameters was found to describe the contaminated materials with the exception of the exchangeable fraction (Table 5). For obvious reasons, the exchangeable fraction was found to be a key variable, as it determined the total amount of Cs^+ that was desorbable from the solid. Equilibrium model calculations (not shown) indicated that the mass action pressure of both 2 mol/L KNO_3 and $RbNO_3$ was sufficient to displace all exchangeable Cs^+ from high affinity sites, if mass action equilibrium was achieved. Therefore, the total desorbed Cs^+ after 70 d was approximately equal to the exchangeable concentration, plus a small amount residual concentration bound to intraparticle high affinity sites that have not yet diffused to the aqueous phase. Consistent with the attainment of a common, final desorbed concentration for sample 7A in KNO_3 and $RbNO_3$ electrolytes (Fig. 13b), the computed exchangeable fraction in both electrolytes was approximately the same (e.g., 35%). The smaller increase in Cs^+ desorption that was observed after the increase in concentration of $RbNO_3$ from 0.5 to 2 mol/L (compared to KNO_3) was therefore interpreted as resulting from a global depletion in exchangeable Cs^+

Table 5. Parameters used in diffusion modeling.

	Uncontaminated sediment			
Electrolyte	D/L^2 (day^{-1})	b[a]	E^{ext}/E^{in} [b]	E^{in+ext}
$NaNO_3$	9.0×10^{-2}	0.05	0.61	4.5×10^{-4}
KNO_3	2.5×10^{-4}	0.05	0.50	4.5×10^{-4}
$RbNO_3$	2.5×10^{-4}	0.05	0.42	4.5×10^{-4}

	$^{137}Cs^+$-contaminated sediment				$^{137}Cs^+$ (exe/tot)[c]	
Sample	D/L^2 (day^{-1})	b[a]	E^{ext}/E^{in} [b]	E^{in+er}	KNO_3	$RbNO_3$
SX-108 3A	2.5×10^{-4}	0.05	0.84	5.7×10^{-4}	0.45	0.32
SX-108 7A	2.5×10^{-4}	0.05	0.84	5.7×10^{-4}	0.37	0.34
41-09-39 7A/B/C	2.5×10^{-4}	0.05	0.84	5.7×10^{-4}	0.44	0.43
41-09-39 9A/B/C	2.5×10^{-4}	0.05	0.84	5.7×10^{-4}	0.45	0.42

[a] b is a parameter for the shape of intraparticle density function (see text).
[b] Ratio of external vs. intraparticle high affinity sites.
[c] Ratio of exchangeable $^{137}Cs^+$ (equilibrium + kinetic) to total $^{137}Cs^+$.

on high affinity sites. In contrast, the larger total desorbed Cs^+ concentration for sample 3A in KNO_3 (Fig. 13) implied that the exchangeable fraction was significantly higher in KNO_3 than in $RbNO_3$ electrolyte (Table 5). This difference may result from interlayer collapse in $RbNO_3$, or other unknown factors.

5. CONCLUSIONS

We have studied the desorption of Cs^+ from pristine/laboratory-spiked and contaminated subsurface sediment samples from the U.S. DOE Hanford site. Over 2 million Ci of $^{137}Cs^+$ has been released to vadose zone sediments at this site in the form of leaked high-level nuclear waste, and considerable concern exists with regard to the future migration of sorbed, in-ground residuals. Desorbability is a key factor governing future migration. The $^{137}Cs^+$-containing sediments studied here were contaminated over 30 yr ago through accidental leakage of a caustic, hot brine containing approximately $10^{-4.5}$ mol/L $^{137}Cs^+$.

Sodium, K^+, Rb^+, and NH_4^+ electrolytes, and a selective Cs^+ sorbent were used to desorb adsorbed Cs^+ through ion exchange mass action. Approximately 40% of the adsorbed pool was exchangeable (equilibrium plus kinetic). This percentage increased to 60–80% after long-term contact with acidified ammonium oxalate (AAO). AAO was thought to increase Cs^+ desorption through the dissolution of microscopically thin, edge regions of phyllosilicates where high-affinity frayed edge sites are believed to reside. Four different contaminated sediment samples were studied that were collected at different (e.g., increasing) distances from the leaked, single shell waste tank. All the sediments exhibited common behavior.

Relative to the equilibrium state, Na^+ was the most effective desorbing cation. Desorption studies with Cs^+-spiked pristine sediment equilibrated for short duration indicated that adsorbed Cs^+, that was fully exchangeable in Na^+ electrolyte, became less exchangeable when placed in K^+ and Rb^+ electrolyte. This effect was attributed to the collapse of edge and partially expanded interlamellar regions resulting from saturation of the exchange complex with poorly hydrated K^+ and Rb^+ cations.

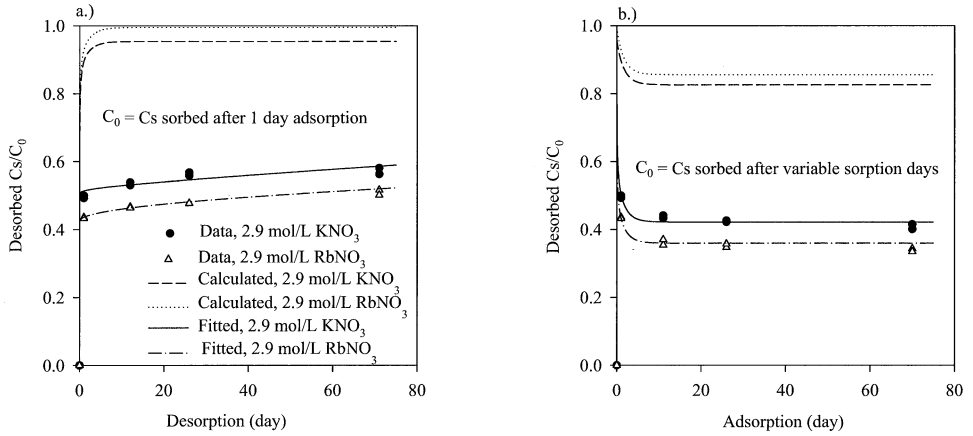

Fig. 12. Results of the coupled model of intraparticle diffusion with two-site external equilibrium ion exchange. Predicted and fitted desorption in 2.9 mol/L KNO_3 and $RbNO_3$ after 1 d adsorption (Fig. 12a), and 1 d of desorption after variable days of adsorption (Fig. 12b).

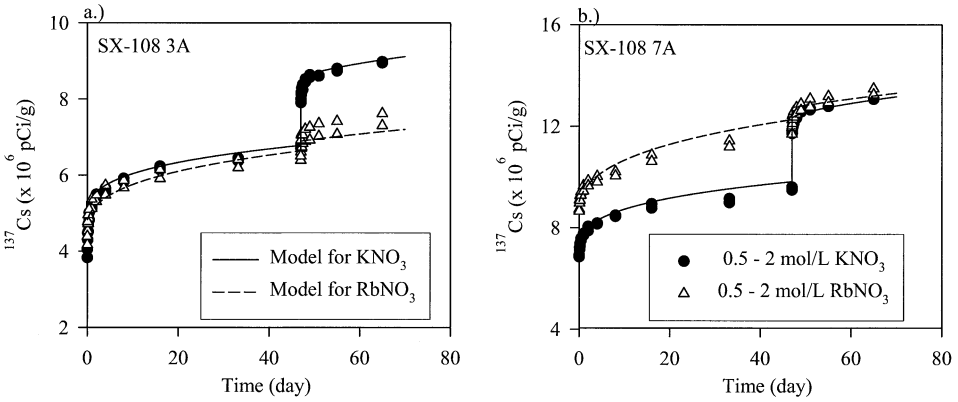

Fig. 13. Modeling results of the Cs^+ desorption from the Cs^+-contaminated Hanford sediments using the coupled model of intraparticle diffusion with two-site external equilibrium ion exchange in 0.5–2 mol/L KNO_3 and $RbNO_3$ electrolytes.

Such collapse decreased the intraparticle diffusivity of adsorbed Cs^+ by many orders of magnitude. Desorption studies with the contaminated sediments in these same electrolytes showed evidence for collapse at higher electrolyte concentrations of K^+ and Rb^+. Collapse lead to a significant decrease in the apparent exchangeable fraction.

X-ray microprobe measurements of Cs^+-sorbed mica from the pristine sediment showed Cs^+ in complex intraparticle distribution. Cesium was localized to select edge region, to the particle periphery, and also to internal channels running in parallel to the basal plane believed to be cleavage fractures. We assumed this distribution to be representative of micaceous mineral sorbents in the contaminated sediments, but were unable to verify by direct measurement. This particle distribution was amenable to description with a slab diffusion transport model that was linked to a two-site ion exchange model. The desorption resistant fraction that was not explicitly considered in this model, representing approximately 60% of the total adsorbed pool, has likely diffused into 1.0 nm phyllosilicate regions with dominant K^+ saturation.

Our results have shown that a minimum of 24% of the adsorbed Cs^+ pool in the contaminated sediment is responsive to ion exchange mass action with aqueous electrolyte cations. The exchangeable fraction varies up to 56.4% depending on the nature of the electrolyte cation and its concentration. Accurate in-situ calculations of desorption in these particular sediments requires explicit consideration of K^+ concentrations in the aqueous and exchanger phase because of its potential to collapse edge and interlamellar regions with attendant effects on $^{137}Cs^+$ exchangeability and intraparticle diffusivity.

Acknowledgments—This research was supported by the U.S. Department of Energy (DOE) through the Environmental Management Sciences Program (EMSP) and the Hanford Science and Technology Program managed by the Groundwater Protection Project. Pacific Northwest National Laboratory (PNNL) is operated for the DOE by Battelle Memorial Institute under contract DE-AC06-76RLO 1830. We thank Dr. Y. Lin at PNNL for providing SAMMS materials. We also thank two reviewers for their valuable comments and suggestions.

Associate editor: J. D. Rimstidt

REFERENCES

Ball W. P. and Roberts P. V. (1991) Diffusive rate limitations in the sorption of organic chemicals. In *Organic Substances and Sediments in Water: Processes and Analytical*, Vol. 2 (ed. R. A. Baker), pp. 273–310. Lewis Publishers.

Barrer R. M. and Klinowski J. (1974) Ion-exchange selectivity and electrolyte concentration. *J. Chem. Soc. Farad. Trans. I* **70**, 2080–2091.

Brouwer E., Baeyens B., Maes A., and Cremers A. (1983) Cesium and rubidium ion equilibria in illite clay. *J. Phys. Chem.* **87**, 1213–1219.

Comans R. N. J., Haller M., and De Preter P. (1991) Sorption of cesium on illite: Non-equilibrium behavior and reversibility. *Geochim. Cosmochim. Acta.* **55**, 433–440.

Comans R. N. J. and Hockley D. E. (1992) Kinetics of cesium sorption on illite. *Geochim. Cosmochim. Acta* **56**, 1157–1164.

Cornell R. M. (1993) Adsorption of cesium on minerals: A review. *J. Radioanal. Nucl. Chem. Articles* **171**, 483–500.

Cowan C. E., Zachara J. M., and Resch C. T. (1991) Cadmium adsorption on iron oxides in the presence of alkaline-earth minerals. *Environ. Sci. Technol.* **25**, 437–446.

Cremers A., Elsen A., De Preter P., and Maes A. (1988) Quantitative analysis of radiocesium retention in soils. *Lett. Nat.* **335**, 247–249.

Cussler E. L. (1995) *Diffusion: Mass Transfer in Fluid Systems*. Cambridge University Press.

De Preter P. (1990) Radiocesium retention in the aquatic, terrestrial and urban environment: A quantitative and unifying analysis. Katholieke Unversiteit. Ph.D dissertation.

Di Toro D. M., Mahoney J. D., Kirchgraber P. R., O'Byrne A. L., Pasquale L. R., and Piccirilli D. C. (1986) Effects of nonreversibility, particle concentration and ionic strength on heavy metal sorption. *Environ. Sci. Technol.* **20**, 55–61.

Do D. D. (1998) *Adsorption Analysis: Equilibrium and Kinetics*. Imperial College Press.

Eberl D. D. (1980) Alkali cation selectivity and fixation by clay minerals. *Clays Clay Miner.* **28**, 161–172.

Evans D. W., Alberts J. J., and Clark R. A. (1983) Reversible ion-exchange fixation of cesium-137 leading to mobilization from reservoir sediments. *Geochim. Cosmochim. Acta* **47**, 1041–1049.

Evans J. C., Dresel P. E., Farmer O. T., Conrad M. S., and DePaolo D. J. (2001) Transport mechanisms inferred by isotope geochemistry. In *Digest of S&T Program Evaluations, S-SX FIR Appendix D*, pp. D227–D240. Pacific Northwest National Laboratory.

Felmy A. R. (1995) GMIN, A computerized chemical equilibrium program using a constrained minimization of the Gibbs free energy: Summary report. In *Chemical Equilibrium and Reaction Models* (eds. R. H. Loeppert, A. P. Schwab, and S. Goldberg) pp. 377–407. Soil Science Society of America.

Kim Y., Cygan R. T., and Kirkpatrick R. J. (1996) ^{133}Cs NMR and XPS investigation of cesium adsorbed on clay minerals and related phases. *Geochim. Cosmochim. Acta* **60**, 1041–1052.

Le Roux J., Rich C. I., and Ribbe P. H. (1970) Ion selectivity by weathered mica as determined by electron microprobe analysis. *Clays Clay Miner.* **18**, 333–338.

Lin Y., Fryxell G. E., Wu H., and Engelhard M. (2001) Selective sorption of cesium using self-assembled monolayers on mesoporous supports. *Environ. Sci. Technol.* **35**, 3962–3966.

Liu D.-C., Hsu C. N., and Chung C. L. (1994) Ion-exchange and sorption kinetics of cesium and strontium in soils. *Appl. Radiat. Isotopes* **46**, 839–846.

Liu C., Zachara J. M., and Smith S. C. (2003) A cation exchange model to describe Cs sorption at high ionic strength in subsurface sediments at Hanford site, USA. *J. Contam. Hydrol.*,in press.

Loeppert R. L. and Inskeep W. P. (1996) Iron. In *Methods of Soil Analysis, Part 3—Chemical Methods*, Vol. 5 (eds. D. L. Sparks et al.), pp. 639–664. Soil Science Society of America.

McKinley J. P., Zeissler C. J., Zachara J. M., Serne R. J., Lindstrom R. M., Schaef H. T., and Orr R. D. (2001) Distribution and retention of ^{137}Cs in sediments at the Hanford site, Washington. *Environ. Sci. Technol.* **35**, 3433–3441.

Pitzer K. S. (1994) *Ion Interaction Approach: Theory and Data Correlation*. CRC Press.

Poinssot C., Baeyens B., and Bradbury M. H. (1999) Experimental and modeling studies of cesium sorption on illite. *Geochim. Cosmochim. Acta* **63**, 3217–3227.

Sawhney B. L. (1967) Interstratification in vermiculite. *Clays Clay Miner.* **15**, 75–84.

Sawhney B. L. (1969) Regularity of interstratification as affected by charge density in layer silicates. *Soil Sci. Soc. Am. Proc.* **33**, 42–46.

Sawhney B. L. (1972) Selective sorption and fixation of cations by clay minerals: A review. *Clays Clay Miner.* **20**, 93–100.

Serne R. J., Last G. V., Gee G. W., Schaef H. T., Lanigan D. C., Lindenmeier C. W., Clayton R. E., LeGore V. L., Orr R. D., O'Hara M. J., Brown C. F., Burke D. B., Owen A. T., Kutnyakov I. V., and Wilson T. C. (2001a) *Geologic and Geochemical Data Collected from Vadose Zone Sediments from Borehole SX 41-09-39 in the S/SX Waste Management Area and Preliminary Interpretations.*Pacific Northwest National Laboratory.

Serne R. J., Schaef H. T., Last G. V., Lanigan D. C., Lindenmeier C. W., Clayton R. E., LeGore V. L., O'Hara M. J., Brown C. F., Orr R. D., Kutnyakov I. V., Wilson T. C., Burke D. B., Williams B. A., and Bjornstad B. N. (2001b) *Geologic and Geochemical Data Collected from Vadose Zone: Sediments from the Slant Borehole under SX-108 in the S/SX Waste Management Area and Preliminary Interpretations.*Pacific Northwest National Laboratory.

Smith J. T. and Comans R. N. J. (1996) Modeling the diffusive transport and remobilization of ^{137}Cs in sediments: The effects of sorption kinetics and reversibility. *Geochim. Cosmochim. Acta.* **60**, 995–1004.

Sposito G. (1994) *Chemical Equilibria and Kinetics in Soils*. Oxford Clarendon Press.

Steefel C., Carroll S., Zhao P., and Roberts S. (2002) Reactive transport experiments investigating the migration of ^{137}Cs in sediments beneath the Hanford SX tank farm. *J. Contam. Hydrol.*, in press.

Weiss C. A., Kirkpatrick R. J., and Altaner S. P. (1990a) The structural environments of cations adsorbed onto clays: ^{133}Cs variable-temperature MASA NMR spectroscopic study of hectorite. *Geochim. Cosmochim. Acta* **54**, 1655–1669.

Weiss C. A., Kirkpatrick R. J., and Altaner S. P. (1990b) Variations in interlayer cation sites of clay minerals as studied by ^{133}Cs MAS nuclear magnetic resonance spectroscopy. *Am. Mineral.* **75**, 970–982.

Zachara J. M., Smith S. C., Liu C., McKinley J. P., Serne R. J., and Gassman P. L. (2002) Sorption of Cs^+ to micaceous subsurface sediments from the Hanford site, USA. *Geochim. Cosmochim. Acta* **66**, 193–211.